



Vehicle Sideslip Angle estimation under critical road conditions via nonlinear Kalman filter-based state-dependent Interacting Multiple Model approach

Francesco Tufano ^a, Dario Giuseppe Lui ^{a,*}, Simone Battistini ^b, Renato Brancati ^a, Basilio Lenzo ^c, Stefania Santini ^a

^a University of Naples Federico II, Naples, 80125, Italy

^b MBDA Italy SpA, Rome, 00131, Italy

^c University of Padua, Padua, 35131, Italy

ARTICLE INFO

Keywords:
Interacting Multiple Model
Kalman filter
Vehicle Sideslip Angle
Automotive simulation models

ABSTRACT

The knowledge of Vehicle Sideslip Angle (VSA) can play an essential role in active safety vehicle control systems. However, due to the high costs of sensing instruments, this information is difficult to be directly measured onboard of series production vehicles, restricting *de facto* its application in practice. It follows that there is a need for online VSA estimation methods only based on available measurements from low-cost sensors. From this perspective, this work proposes a strategy based on Interacting Multiple Model (IMM) filters, which does not require tyre-road friction coefficient knowledge. By integrating the available onboard sensor data, the IMM estimates relevant information in different driving conditions leveraging a 2-Degrees Of Freedom (DOF) single-track vehicle model embedding a Dugoff tyre representation. Two alternative IMM algorithms based on the Extended (EKF) and Unscented Kalman filter (UKF) are developed. Moreover, while usually the transition probabilities among models in classical IMMs are fixed and set on prior information and/or dedicated analysis, here these conservative hypotheses are relaxed introducing a state-dependent Markov transition matrix based on a novel model switching algorithm. The effectiveness of the new proposed methods is evaluated on extensive non-trivial simulation scenarios through a Monte Carlo analysis exploiting an accurate 15-DOF vehicle model via a purposely designed high-fidelity co-simulation platform embedding the dSPACE software Automotive Simulation Model (ASM). Results provide a meaningful comparative performance analysis between the IMMEKF and IMMUKF solutions, as well as with respect to traditional IMM based on constant probabilities transition matrix, blue in both the EKF and UKF configuration. Finally, the developed IMM-based estimation strategy is tested in two realistic driving scenarios to assess the VSA estimation accuracy in case of abrupt changes in road surface conditions.

1. Introduction

Advanced Driver-Assistance Systems (ADAS) and Autonomous Driving Systems (ADS) have received significant research attention due to their potential benefits in achieving the goals of sustainable mobility in the future (Coppola, Lui, Petrillo, & Santini, 2021), since they are suitably designed to automate, adapt, and enhance vehicle technology for safety fuel-efficient driving (Eco-Driving) (e.g., see Caiazzo, Lui, Petrillo, and Santini (2021), Coppola, Lui, Petrillo, and Santini (2022), Di Vaio et al. (2019), Musa et al. (2021) and references therein). In this perspective, a proper control system should rely on the exploitation of a large amount of information (Petrillo, Prati, Santini, & Tufano, 2023), such as yaw rate, sideslip angle, and longitudinal and/or lateral velocity, just to name a few. However, a high-performance full sensor

set is not practically attainable in commercial cars, mainly due to the high costs of this sensing system. It follows that state estimation methods based on low-cost sensors have been widely exploited and applied in the automotive industry to replace accurate measurement information, e.g. for path planning, decision making, active safety controller design of intelligence vehicles (Fiengo, Lui, Petrillo, Santini, & Tufo, 2019).

The Vehicle Sideslip Angle (VSA), (i.e. the angle between the longitudinal direction of the vehicle and the velocity vector), represents an indicator of how much the vehicle slides sideways when cornering (Park, 2022) and is one of the most important variables used in developing a large number of active safety vehicle systems. Despite

* Corresponding author.

E-mail addresses: francesco.tufano@unina.it (F. Tufano), dariogiuseppe.lui@unina.it (D.G. Lui), simone.battistini@mbda.it (S. Battistini), renato.brancati@unina.it (R. Brancati), basilio.lenzo@unipd.it (B. Lenzo), stefania.santini@unina.it (S. Santini).

its importance this information is not commonly directly measured onboard in series production vehicles since it can be correctly sensed by means of high-cost sophisticated laboratory devices (e.g., optical sensors such as the Corrysys-Datron Chindamo, Lenzo, & Gadola, 2018) - that present issues in terms of compatibility with vehicle packaging, cost, reliability, accuracy, and robustness to environmental conditions. So, the proper onboard estimation of VSA could be therefore a promising solution due to its high potential in improving the performance of vehicle motion control systems, such as stabilization and path tracking capabilities or vehicle lateral control stability in critical driving conditions (Madhusudhanan, Corno, & Holweg, 2016; Park, 2022). The literature overview on the VSA estimation has been well documented in Chindamo et al. (2018) which suggests categorizing the approaches into four main groups: kinematics and dynamics vehicle-based approaches, a combination of them, and the learning-based methods. Specifically, kinematics-based estimation methods have raised a large interest since they do not require vehicle parameters, tyre models, and road friction coefficient. Liao and Borrelli (2019), Selmanaj, Corno, Panzani, and Savaresi (2017) and it provides an accurate estimation in different driving cases. However, they are reliable only for transient manoeuvres due to the progressive integral drifting caused by sensor errors (Li & Zhang, 2016) and suffer from disturbance and measurement noise. The dynamics-based methods, instead, exploit the vehicle model and, as such, suffer particularly the model errors, the uncertainties, and the discrepancies when the manoeuvres with high lateral excitations occur (Xia et al., 2021). To compensate for these deficiencies, a combination of both methodologies can be considered (Xia et al., 2021), but the performance could be poor if not all suitable information is considered. Finally, learning-based techniques are model-free (Bonfitto, Feraco, Tonoli, & Amati, 2020) and independent of sensor errors (de Nola et al., 2017) since they exploit deep neural networks and their capability of serving as universal function approximator (Candeli et al., 2022), but their main drawback is the low reliability of the estimate when conditions are not sufficiently close to the ones of the training set (Chindamo et al., 2018).

This last issue still makes the model-based estimation methods an attractive solution to be adopted. To this aim, Kalman Filter (KF) theory has been widely employed in the technical literature in different research fields, where several well-assessed approaches have been proposed (Chindamo et al., 2018). However, when the vehicle dynamics are characterized by great complexity and vary unexpectedly due to unknown inputs, as for the case of the tyre-road friction coefficient, an estimator based on a single dynamical model can exhibit poor closed-loop performance (Ray, 1997). To deal with this critical aspect, estimators based on Multiple Models (MMs), designed according to different vehicle behaviours according to specific characteristics of road surface conditions, could lead to more accurate estimation performance than a trivial single model solution (Tsunashima, Murakami, & Miyataa, 2006).

Out of the various solutions based on the MM paradigm, the Interacting Multiple Model (IMM) algorithms are very popular due to their high accuracy, cost-effectiveness, and low computational burden, which make it particularly suitable for the implementation in real-time in electronic control units (ECU) of general mass production vehicles (Blom, 1984). Moreover, the approach exhibits suitable robustness performance and allows to maintain high estimation accuracy due to the multiple model combination which attributes a higher weight to the more accurate vehicle model in real time (Park, 2022). Indeed, due to these features, the IMM has become the mainstream solution for the state estimation problem and has been often applied for solving different issues such as manoeuvring target tracking, fault detection and diagnosis, and navigation (eg. see Menegaz and Battistini (2018) and references therein).

The usual IMM structure is composed of a bank of multiple filters, each set on a specific dynamical model, that operates in parallel to obtain a better state estimate (Joa, Yi, & Hyun, 2019). Note that the

state-of-art proposes different versions of the IMM, ranging from the use of linear KF to its nonlinear extensions, e.g., Extended Kalman Filter (EKF) (Tsunashima et al., 2006), (Strano & Terzo, 2018), Unscented Kalman Filter (UKF) (Brancati & Tufano, 2022), Adaptive parameter Unscented Filter (AUF) (Xu et al., 2022), and so on. Then, a model management algorithm, governed by an underlying Markov transition matrix, is in charge of the switching behaviour among the multiple models.

Regardless of the adopted solution (e.g., EKF, UKF, or AUF), the Transition Probability Matrix (TPM) has a crucial role in the definition and operation of the IMM algorithm, and its tuning remains a difficult task to be accomplished by leveraging *a priori* information and/or dedicated analysis. Therefore, the usual solution adopted in the current literature considers the probabilities of the state transitioning among models as constant values. However, this setting method tends to be quite conservative and degrades the estimation accuracy of the IMM system, since it relies on two strong hypotheses, namely: (i) the assumption that the state-dependent probability of the TPM transitioning among models can be well represented by a constant value; (ii) this constant probability value is *a priori* known. Indeed, if the transition probabilities could be adapted online according to the current system model information, the performance of the IMM algorithm can be significantly improved. Examples can be found in the aeronautic field where the target tracking of kinematic variables of ballistic missiles has been often improved by exploiting different TPM with state-dependent probabilities of the state transitioning that relies on physical considerations on the phases of flight (e.g., see Battistini and Menegaz (2017), Menegaz and Battistini (2018), Guo, Dong, Cai, and Yu (2015), Xie, Sun, Wen, Hei, and Qian (2019) and references therein.)

Motivated by the above discussion and the well-investigated capability of IMM solutions in providing good estimating performance in challenging conditions, this article proposes two novel IMM-based estimation systems for VSA, namely based on Extended and Unscented Kalman Filter theory, equipped with a state-dependent Markov Transition Probability Matrix able to adapt online its probabilities according to the current system via a novel model switching algorithm. In so doing, it is possible avoiding dedicated analysis and/or exploitation of any *a priori* information. Comparison analysis between the IMMEKF and IMMUKF is also carried out to evaluate the benefits of both solutions in terms of estimation performance, as well as with respect to a classical IMM with constant TPM.

The effectiveness of the theoretical framework has been then confirmed in realistic driving conditions emulated leveraging a purposely designed high-fidelity co-simulation platform embedding the industrial software dSPACE Automotive Simulation Models (ASM). Results disclose the ability of the proposed solution in non-trivial and realistic driving environments. Note that the interest in high-fidelity environment platforms is getting higher and higher in automotive. Of course, "modelling" plays a central role in the development of embedded control systems where some simplifications are crucial to perform the control design phase (e.g., neglecting disturbances or nonlinear dynamics hard to handle, and so on). Simplifications clearly introduce mismatches between the model and the real plant and it follows that is critical for automotive companies to validate any system via high-fidelity simulation platforms reproducing realistic driving conditions, allowing not only to reduce the number of test drives but also to reproduce a wide range of scenarios (ODDs, Operational Design Domains), especially the ones including emerging dangerous situations which are impossible to be safely assessed in the real world (Jasiński, 2019). Illustrating this point, research by Chowdhri, Ferranti, Iribarren, and Shyrokau (2021) has leveraged a high-fidelity vehicle simulator to assess an integrated nonlinear Model Predictive Control (MPC) controller. This controller is adept at maintaining effective vehicle control in both linear and nonlinear motion regimes and is instrumental in reducing accidents, particularly in rear-end collision scenarios. Similarly, Jing,

[Shu, Shu, and Song \(2022\)](#) have employed simulation techniques to ascertain the effectiveness of an integrated control strategy. This strategy synergizes yaw stability and energy efficiency, combining MPC with an active steering system. Herein, reflecting the prevalent practice of employing simulation-based testing for the assessment of algorithms designed for vehicle control systems, a realistic and high-fidelity platform, embedding the well-known dSPACE ASM software, is exploited to emulate the ego-vehicle and the nearby environment, so as to deeply evaluate the efficiency of the proposed estimating strategies in different driving conditions.

Finally, the main contributions of this paper can be summarized as follows.

- Unlike classic approaches leveraging a single-model filter, the proposed VSA estimation algorithm based on an adaptive IMM approach is able to cope with different road surface conditions. In doing so, the proposed method turns out to be not only the best cost-effectiveness solution ([Xie et al., 2019](#)), but the lower computational burden makes it particularly suitable for the implementation in real-time in electronic control units (ECU) of general mass production vehicles ([Blom, 1984](#)).
- The online estimation exploits a two Degrees Of Freedom (2-DOF) single-track vehicle model embedding a Dugoff tyre representation, whose parameters have been selected according to four different tyre-road friction scenarios. This allows adaptively identifying the current VSA avoiding difficult online evaluation of tyre-road contact model parameters ([Di Biase, Lenzo, & Timpone, 2020](#); [Ping et al., 2020](#)).
- The state-dependent TPM is able to realize online learning via a novel model switching algorithm, without any *a priori* information, allowing a greatly improve performance without increasing computational load. Furthermore, while generally TPMs are assumed constant and their values are chosen based on well-known information and/or dedicated analysis ([Jin & Yin, 2015](#); [Xie et al., 2019](#)), that are challenging in the VSA case, in this work this complex analysis is completely avoided, simplifying the algorithm set-up without sacrificing the required estimation performance.
- Two different IMM filter solutions based on the nonlinear Kalman estimation technique are presented and compared. The first is based on the EKF, while the second leverages the UKF. Their performance has been assessed in non-trivial driving scenarios in comparison with respect to an IMM with constant TPM, as well as with EKF and UKF filters solutions, so to justify the multiple models approach adopted. The test manœuvres include the ramp steer and the double-lane change, widely applied in the automotive context in order to assess the handling and performance characteristics of road vehicles ([Demerly & Youcef-Toumi, 2000](#)).
- The solution that exhibited the best performing has been also tested in realistic driving environments via a high-fidelity co-simulation platform based on the Automotive dSPACE ASM vehicle dynamics simulation tool, to assess the VSA estimation accuracy in case of abrupt changes in the road surface conditions. A comparison with an IMM with constant TPM and Kalman filters solutions, i.e. EKF and UKF, further confirm the estimation skill of the proposed nonconstant IMM.

Finally, the paper is structured as follows: the vehicle nonlinear dynamics model is described in Section 2; Section 3 provides the general IMM theory and the application in the vehicular context, explaining the proposed time-varying switching algorithm and the generation of the lateral acceleration which is at its basis; Section 4 is dedicated to the description of the high-fidelity simulation platform, while extensive non-trivial simulations scenarios are discussed in Section 5; conclusions are drawn in Section 6.

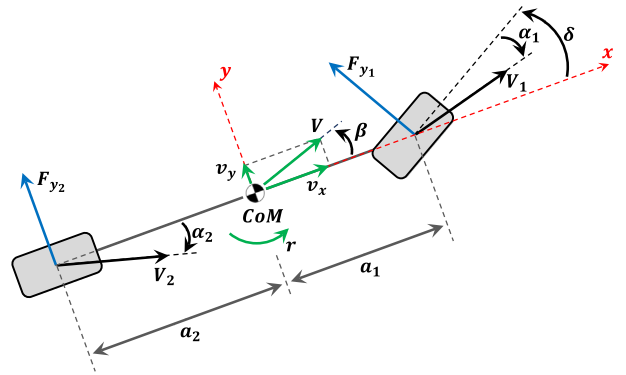


Fig. 1. Schematics of the 2-DOF single-track vehicle model.

2. Vehicle dynamics modelling

Since an overly complex vehicle model is not beneficial for on-line real-time VSA estimation purposes, herein the evaluation procedure funds on a simple 2-DOF single-track vehicle lateral motion model ([Guiggiani, 2014](#)) as schematized in Fig. 1. Considering lumped lateral tyre forces for each axle, say F_{y_i} [N], where $i \in \{1, 2\}$ indicates front and rear respectively, two equilibrium equations can be derived as:

$$m(\dot{v}_y + v_x r) = F_{y_1} + F_{y_2} \quad (1)$$

$$J_z \dot{r} = F_{y_1} a_1 - F_{y_2} a_2, \quad (2)$$

where v_x [m/s] and v_y [m/s] are the longitudinal and lateral velocity, respectively, r [deg/s] is the yaw rate, m [kg] is the vehicle mass, J_z [kg m²] is the inertia moment of the vehicle about the z -axis, and a_i ($i \in \{1, 2\}$) [m] are the semi-wheelbases. Tyre slip angles for the front and rear wheels α_i ($i \in \{1, 2\}$) [deg] are defined in tyre coordinate frames as:

$$\alpha_1 = \delta - \frac{v_y + r a_1}{v_x} \frac{180}{\pi}, \quad \alpha_2 = -\frac{v_y - r a_2}{v_x} \frac{180}{\pi}, \quad (3)$$

being δ [deg] the front wheel steering angle.

Assuming small variations of the slip angle, the dynamic of the lateral forces F_{y_i} can be approximated by the following first-order differential equation ([Doumiati, Victorino, Charara, & Lechner, 2010](#)):

$$\dot{F}_{y_i} = \frac{v_x}{L_{y_i}} (\bar{F}_{y_i} - F_{y_i}), \quad (4)$$

where L_{y_i} ($i \in \{1, 2\}$) [m] are the lateral relaxation lengths and \bar{F}_{y_i} ($i \in \{1, 2\}$) [N] are the steady-state tyres lateral forces. Specifically, \bar{F}_{y_i} are evaluated via the Dugoff quasi-static nonlinear tyre model ([Villano, Lenzo, & Sakhnevych, 2021](#)), i.e.:

$$\bar{F}_{y_i} = C_{\alpha_i} \tan(\alpha_i) p(\lambda_i) G_{\alpha_i}, \quad (5)$$

where C_{α_i} ($i \in \{1, 2\}$) [N/deg] are the cornering stiffness; $p(\lambda_i)$ is the following nonlinear function

$$p(\lambda_i) = \begin{cases} (2 - \lambda_i) \lambda_i, & \text{if } \lambda_i < 1 \\ 1, & \text{if } \lambda_i \geq 1 \end{cases} \quad (6)$$

and

$$G_{\alpha_i} = (c_{f,max} - 1.6) |\tan(\alpha_i)| + 1.155 \quad i \in \{1, 2\}, \quad (7)$$

being

$$\lambda_i = \frac{c_{f,max} F_{z_i}}{2 |C_{\alpha_i} \tan(\alpha_i)|} \quad i \in \{1, 2\}, \quad (8)$$

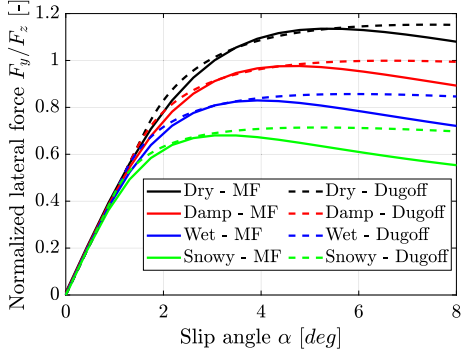


Fig. 2. Normalized lateral tyre force versus tyre slip angle computed using the Magic Formula (MF) 6.1 tyre model (solid lines) and the Dugoff's tyre model (dashed lines).

while F_{z_i} ($i \in \{1, 2\}$) [N] and $c_{f,max}$ [-] are the tyres vertical forces and the friction coefficient, respectively.

Finally, the dynamics related to lateral position y [m] and the yaw angle φ [deg] can be derived as:

$$\dot{y} = v_x \sin \varphi + v_y \cos \varphi \quad (9)$$

$$\dot{\varphi} = r. \quad (10)$$

Eqs. (1), (2), (4), (9) and (10) represent the vehicle dynamic model that will be embedded in the IMM structure whose parameters should be properly chosen so to mimic the behaviour of a specific vehicle while driving in different road surface conditions.

From this perspective, it is worth noting that road conditions strongly affect vehicle dynamics. Indeed, the tyre-road friction coefficient is crucial for understanding actual traction capability and hence, for enhancing vehicle control and stability during acceleration, cornering, and braking under various road surface conditions. For example, Fig. 2 discloses the normalized lateral tyre force for different road conditions (namely, dry, damp, wet, snowy) computed leveraging the well-known Magic Formula (Pacejka, 2005) and the simpler, but effective, Dugoff's model (5), where the Dugoff's model parameters C_{a_i} ($i \in \{1, 2\}$) and $c_{f,max}$ have been assessed by first evaluating the axles characteristic as in Guiggiani (2014) and Pacejka (2005) and then deriving their values according to the approach presented in Dugoff, Fancher, and Segel (1970). Curves therein show how the normalized lateral tyre force is proportional to the slip angle for small values of slip, while, as the slip angle increases the behaviour becomes more and more nonlinear, since saturation occurs. This behaviour confirms that the knowledge of the unknown *a priori* tyre-road friction coefficient is a crucial factor to handle the actual traction capability, so justifying the need for an effective online nonlinear estimator.

3. VSA online estimation via IMM

In this section, the methodology proposed for tackling and solving the online VSA estimation problem under changing driving conditions is detailed. The overall IMM scheme is depicted in Fig. 3, where two different filters, based on the Extended and Unscented Kalman Filters, have been proposed as estimators for the VSA. Indeed, as mentioned in the previous section, the nonlinear nature of the vehicle dynamics, especially under varying road conditions or extreme driving scenarios, requires the design of multiple decoupled nonlinear filters as the base for the IMM algorithm. In this perspective, the EKF is a common widely adopted solution for solving nonlinear estimation applications (Garcia, Pardal, Kuga, & Zanardi, 2019). However, it could bring significant errors when transferring non-linear functions into linear ones via the Taylor series expansion. Conversely, the UKF avoids linearization errors through a direct action on the nonlinear dynamics via the unscented

transformation which, exploiting a set of limited sigma points, allows the calculation of the statistics of a random variable subject to a nonlinear transformation. This feature, in addition to a wide versatility in a broad range of applications, has made the UKF method a powerful tool within the nonlinear estimation theory field, especially in the presence of very strong nonlinearity (Menegaz, Ishihara, Borges, & Vargas, 2015). Given the above reasons, both strategies have been exploited and compared as possible baseline tools for our IMM implementation.

Furthermore, since the IMM structure is characterized by multiple filters that operate in parallel, the actual estimate is obtained through a weighted average leveraging a probabilistic model adopting a Markov Probabilistic Transition Matrix. This step represents a crucial point for the overall estimation process. Indeed, being the IMM a soft handoff algorithm, some estimation issues arise in the presence of system model jumps, especially when these system jumping times are hard to be predicted. Moreover, a strong limitation comes from the common hypothesis that TPM probabilities assume constant values and are set according to well-known *a priori* information and/or careful dedicated analysis. However, these assumptions are in general too conservative and often may result in inaccurate estimation, affecting the overall IMM performance (Battistini, Brancati, Lui, & Tufano, 2022; Xie et al., 2019). So, to overcome these critical issues, herein we propose a mechanism allowing somehow to implement online learning or better adapting of the TPM $\Pi(k)$ probabilities within the IMM.

3.1. IMM design

As commonly done in the traction control field (Battistini et al., 2022), four average road surface conditions are considered, i.e. dry, damp, wet, and snowy. Accordingly, a batch of four nonlinear KFs (corresponding to four different modes) is considered which, as previously mentioned, has been designed following both the EKF and the UKF paradigm (Garcia et al., 2019). Both filters base their functionality on the assumption that the motion, and corresponding measurements, can be represented with sufficient accuracy by different mathematical models (modes) able to witness the changing of the driving conditions according to the road surface. The structure of the IMM is described in Battistini and Menegaz (2017).

The filters' design has been performed in discrete time exploiting the dynamical behaviour of the vehicle obtained by properly discretizing the dynamical system described in Eqs. (1)–(2)–(4)–(9)–(10), as:

$$\begin{aligned} x_k(s_k) &= f_{s_k}(x_{k-1}, u_k) + w_{k-1} \quad s_k \in \{1, \dots, S\} \\ z_k(s_k) &= h_{s_k}(x_k) + v_k, \end{aligned} \quad (11)$$

where k is the time step index, $f_{s_k}(\cdot)$ and $h_{s_k}(\cdot)$ are the process and the measurement nonlinear functions, respectively, $s_k \in \{0, 1, \dots, S\}$ is the state mode at the time instant k , with $S = 4$ being the maximum allowable number of models in our analysis and $k = 1, 2, 3, 4$ to indicate the dry, damp, wet and snowy road conditions, respectively. Moreover, the state vector is defined as $x_k(s_k) = [y_k, v_{y_k}, \varphi_k, r_k, F_{y_{1_k}}(s_k), F_{y_{2_k}}(s_k)]^T \in \mathbb{R}^{6 \times 1}$, where φ_k is the yaw angle, while the measurement vector $z_k(s_k) = [y_k, r_k, a_{y_k}(s_k)]^T \in \mathbb{R}^{3 \times 1}$ includes the lateral displacement y_k , the yaw rate r_k and the lateral acceleration a_{y_k} , provided by the measurement system which integrates the Global Positioning System (GPS), Inertial Measurement Unit (IMU), and all those in-vehicle sensors needed to the aim, with $a_{y_k}(s_k) = (F_{y_{1_k}}(s_k) + F_{y_{2_k}}(s_k))/m$ (Guiggiani, 2014). Note that, it is worth to emphasize that the GPS receiver is available in a cost-effective price range (Yoon & Peng, 2013), and is often integrated into modern vehicles for various applications, including navigation, tracking, and even advanced driver assistance systems (Joubert, Reid, & Noble, 2020). It is worth noting that the lumped lateral tyres forces F_{y_i} ($i \in \{1, 2\}$) are functions of the state mode s_k , so witnessing the changing of the driving conditions according to the road surface. The input vector $u_k = [\delta_{v_k}, v_{x_k}]^T \in \mathbb{R}^{2 \times 1}$ includes

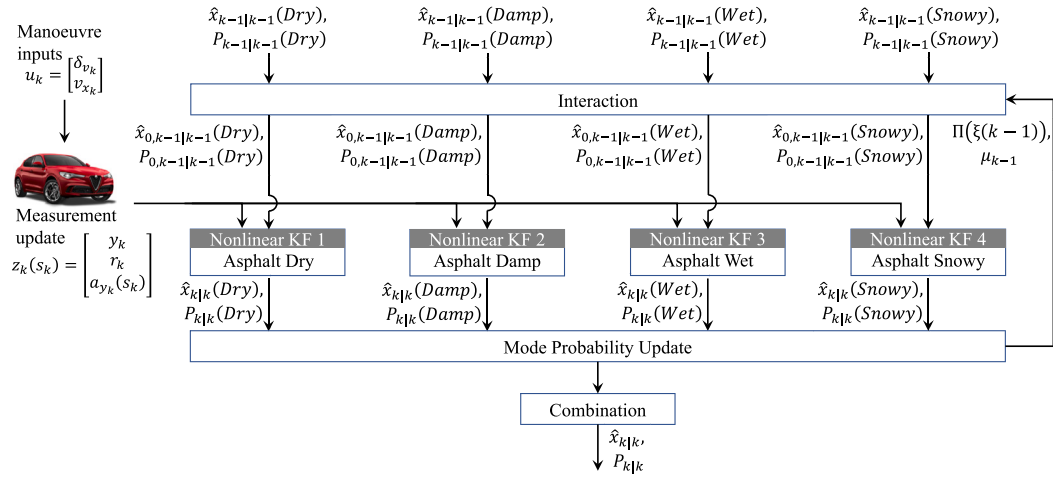


Fig. 3. A block diagram of the proposed state-dependent IMM algorithm based on the nonlinear Kalman estimation theory, IMMEKF or IMMUKF, with four filter models, i.e. dry, damp, wet and snowy road asphalt.

the vehicle longitudinal speed v_{x_k} and the steering angle δ_{v_k} . Finally, as usual, w_{k-1} and v_k are process and measurement uncorrelated noises, both assumed with zero-mean Gaussian distribution with covariance Q_{k-1} and R_k , respectively.

With respect to the structure of $f_{s_k}(\cdot)$ and $h_{s_k}(\cdot)$ in Eqs. (11), this has been derived from the single-track handling dynamics model in Eqs. (1)–(2)–(4)–(9)–(10) by applying the forward Euler method with sampling time Δt , thus yielding:

$$f_{s_k}(\cdot) = \begin{bmatrix} y_{k-1} + \left(v_{x_k} \sin(\varphi_{k-1}) + v_{y_{k-1}} \cos(\varphi_{k-1}) \right) \Delta t \\ v_{y_{k-1}} + \left(\frac{F_{y_{1k-1}}(s_{k-1}) + F_{y_{2k-1}}(s_{k-1})}{m} - v_{x_k} r_{k-1} \right) \Delta t \\ r_{k-1} + \left(\frac{\varphi_{k-1} + r_{k-1} \Delta t}{\frac{F_{y_{1k-1}}(s_{k-1}) a_1 + F_{y_{2k-1}}(s_{k-1}) a_2}{J_z}} \right) \Delta t \\ F_{y_{1k-1}}(s_{k-1}) + \frac{v_{x_k}}{L_{y_1}} \left(\bar{F}_{y_{1k}}(s_k) - F_{y_{1k-1}}(s_{k-1}) \right) \Delta t \\ F_{y_{2k-1}}(s_{k-1}) + \frac{v_{x_k}}{L_{y_2}} \left(\bar{F}_{y_{2k}}(s_k) - F_{y_{2k-1}}(s_{k-1}) \right) \Delta t \end{bmatrix} \quad (12)$$

and

$$h_{s_k}(\cdot) = \begin{bmatrix} z_{1k} \\ z_{2k} \\ z_{3k} \end{bmatrix} = \begin{bmatrix} y_k \\ r_k \\ \frac{F_{y_{1k}}(s_k) + F_{y_{2k}}(s_k)}{m} \end{bmatrix}. \quad (13)$$

Summarizing, the mathematical steps of the IMM algorithm applied are given in Algorithm 1.

Remark 1. Note that, the changing driving conditions affect directly the lumped lateral tyre forces $F_{y_i}(s_k)$, $i = 1, 2$ and this relation is indicated by the state mode variable dependency s_k , with $k = 1, 2, 3, 4$ for the dry, wet, damp and snowy cases, respectively. Since the lateral acceleration can be expressed as a linear combination of these forces (Guiggiani, 2014), consequently the road types influence directly this variable, as also depicted in Fig. 2. According the state and output vectors $x_k(s_k) \in \mathbb{R}^{6 \times 1}$ and $z_k(s_k) \in \mathbb{R}^{3 \times 1}$, respectively, used in the Extended and Unscented Kalman filters, the state mode s_k influences directly the provided estimation according to the driving conditions.

3.2. Markov TPM design

The Markov process is defined via the following TPM matrix $\Pi(k) = [\Pi_{\tau j}(k)]_{S \times S}$ whose elements are:

$$\Pi_{\tau j}(k) = \mathbb{P}\{s_k = j | s_{k-1} = \tau\} \in [0, 1], \quad (14)$$

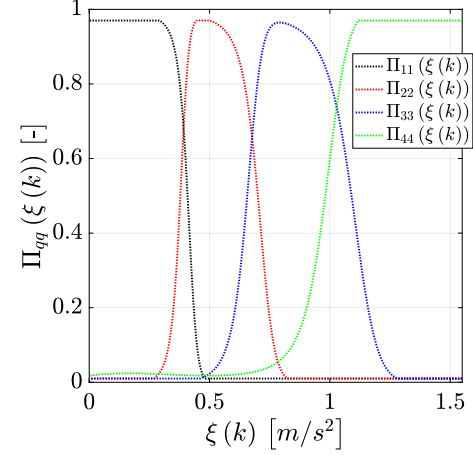


Fig. 4. Diagonal time-varying elements of the transition matrix $\Pi(\xi(k))$.

where, for a given event e , $\mathbb{P}\{e\}$ stands for the probability of occurrence of e and, obviously, $\sum_{j=1}^S \Pi_{\tau j}(k) = 1$, $\tau \in \{1, \dots, S\}$. It is worth noting that, given a time instant k , $\Pi_{\tau j}(k)$ indicates the probability to have model j if at time instant $k-1$ the model was τ .

For determining the model probabilities transitioning, the following switching signal $\xi(k)$, accounting for the deviation of the real lateral acceleration with respect to a reference lateral acceleration obtained in dry road conditions, is defined (Menegaz & Battistini, 2018):

$$\xi(k) = \left| a_{y_k}^{Dry}(\delta_v(k), v_x(k)) - a_{y_k}(s_k) \right|, \quad (15)$$

being $a_{y_k}^{Dry}$ the vehicle reference lateral acceleration under dry road surface conditions at time instant k , suitably preset via a lookup table whose inputs are the current steering angle $\delta_v(k)$ and longitudinal velocity $v_x(k)$, while $a_{y_k}(s_k)$ represents the measurement of the actual lateral acceleration provided by an accelerometer at time k , which is correlated to the actual driving asphalt conditions.

Thus, when the vehicle engages a manoeuvre that entails lateral dynamics, a transition from a dry road surface, the motion from an asphalt condition to another characterized by a lower conditions (e.g. from dry to snowy), introduce several changes the vehicle's lateral response and, consequently, its lateral acceleration. Therefore, a greater discrepancy between the measured lateral acceleration and the reference dry conditions enhances the likelihood that the vehicle is operating on a road surface characterized by a lower coefficient of friction. The sigmoid

Algorithm 1 Interacting Multiple Model (IMM)

1. Interaction. Mixing probabilities $\mu_{\cdot| \cdot}(\tau|j)$ evaluation,

$$\mu_{k-1|k-1}(\tau|j) = \frac{1}{\bar{\eta}(j)} \Pi_{\tau j} \mu_{k-1}(\tau)$$

being $\bar{\eta}(j) = \sum_{\tau=1}^S \Pi_{\tau j} \mu_{k-1}(\tau)$, where, $\mu_{k-1}(\tau)$ is the mode probability at time $k-1$, and $\Pi_{\tau j}$ denotes the state transfer probability from model τ to model j . The mixed initial state condition $\hat{x}_{0,k-1|k-1}(j)$ and covariance $P_{0,k-1|k-1}(j)$ for mode-matched filter j at time $k-1$ are

$$\begin{aligned}\hat{x}_{0,k-1|k-1}(j) &= \sum_{\tau=1}^S \hat{x}_{k-1|k-1}(\tau) \mu_{k-1|k-1}(\tau|j), \\ P_{0,k-1|k-1}(j) &= \sum_{\tau=1}^S \mu_{k-1|k-1}(\tau|j) \left(P_{k-1|k-1}(\tau) \right. \\ &\quad \left. + [\hat{x}_{k-1|k-1}(\tau) - \hat{x}_{0,k-1|k-1}(j)] \cdot [\hat{x}_{k-1|k-1}(\tau) - \hat{x}_{0,k-1|k-1}(j)]^\top \right)\end{aligned}$$

where, $\hat{x}_{k-1|k-1}(\tau)$ denotes the state estimate for mode-matched filter τ at time $k-1$ and $P_{k-1|k-1}(\tau)$ its covariance matrix.

2. Nonlinear estimation via EKF/UKF (Garcia et al., 2019) is used to obtain the posterior state estimation $\hat{x}_{k|k}(j)$, the state covariance matrix $P_{k|k}(j)$, the measurement output $\hat{z}_{k|k-1}(j)$ and the innovation covariance matrix $P_{k|k-1}^{zz}(j)$ for the j -th model.

3. Model probability update. Under the Gaussian assumption, the likelihood function $A(j)$ can be evaluated as a function of the innovation $N(j)$ with respect to measurement z_k

$$A_k(j) = \frac{\exp \left\{ -\frac{1}{2} \left(N_k(j)^\top \left(P_{k|k-1}^{zz}(j) \right)^{-1} N_k(j) \right) \right\}}{\sqrt{2\pi P_{k|k-1}^{zz}(j)}},$$

$$N_k(j) = z_k - \hat{z}_{k|k-1}(j)$$

Then, the model probability is calculated as

$$\mu_k(j) = \frac{1}{\sum_{j=1}^S A_k(j) \bar{\eta}(j)} A_k(j) \bar{\eta}(j)$$

4. Combination. Output interacting is obtained by combining the previous results from each filter, obtaining the state estimation $\hat{x}_{k|k}$ at time k and its covariance $P_{k|k}$ according to

$$\begin{aligned}\hat{x}_{k|k} &= \sum_{j=1}^S \hat{x}_{k|k}(j) \mu_k(j), \\ P_{k|k} &= \sum_{j=1}^S \mu_k(j) \left(P_{k|k}(j) + [\hat{x}_{k|k}(j) - \hat{x}_{k|k}] \cdot [\hat{x}_{k|k}(j) - \hat{x}_{k|k}]^\top \right)\end{aligned}$$

functions have been designed to follow this probability transitioning, in order to assign the 100% of probabilities when the vehicle is driving on road conditions for which the correspondent state-mode is able to perform a reliable estimation, and 0% otherwise. In Fig. 4 are depicted the diagonal values of the state-dependent elements of the Markov transition matrix. For lower values of $\xi(k)$ (e.g. below 0.3 [m/s²]), no appreciable deviations of lateral acceleration with respect to dry reference conditions occur. Accordingly, the sigmoid function corresponding to the state-mode $\Pi_{11}(\xi(k))$ converges approximately to 1, while the others to 0, suggesting a higher probability of encountering a dry road surface. As $\xi(k)$ increases, the sigmoid function of the state mode $\Pi_{11}(\xi(k))$ gradually decreases towards 0, while the state-mode $\Pi_{22}(\xi(k))$ increases, indicating an highest likelihood of encountering a damp road surface condition. For $\xi(k)$ values exceeding 0.7 [m/s²], the sigmoid function values suggest a transition from damp to wet road surface conditions. Furthermore, when $\xi(k)$ exceeds 1, the state-mode associated with snowy asphalt conditions exhibits the highest probability. These four sigmoid functions represents the diagonal elements of the proposed TPM. More specifically, according to (15), the TPM can be defined as a function of $\xi(k)$ for dry, damp, wet, and snowy asphalt

Table 1
Parameters values.

Parameter	Value	Parameter	Value
$d_{1,1}$ [-]	30	$\rho_{1,1}$ [-]	14
$d_{2,1}$ [-]	20	$\rho_{2,1}$ [-]	16
$d_{3,1}$ [-]	40	$\rho_{3,1}$ [-]	5
$d_{4,1}$ [-]	40	$\rho_{4,1}$ [-]	1
$d_{2,2}$ [-]	15	$\rho_{2,2}$ [-]	4
$d_{3,2}$ [-]	50	$\rho_{3,2}$ [-]	1

conditions as:

$$\Pi(\xi(k)) = \begin{bmatrix} \Pi_{11}(\xi(k)) & \Pi_{12}(\xi(k)) & \Pi_{13}(\xi(k)) & \Pi_{14}(\xi(k)) \\ \Pi_{21}(\xi(k)) & \Pi_{22}(\xi(k)) & \Pi_{23}(\xi(k)) & \Pi_{24}(\xi(k)) \\ \Pi_{31}(\xi(k)) & \Pi_{32}(\xi(k)) & \Pi_{33}(\xi(k)) & \Pi_{34}(\xi(k)) \\ \Pi_{41}(\xi(k)) & \Pi_{42}(\xi(k)) & \Pi_{43}(\xi(k)) & \Pi_{44}(\xi(k)) \end{bmatrix} \quad (16)$$

The following sigmoid functions have been used to describe the road conditions probabilities $\Pi_{qq}(\xi(k))$ along the main diagonal:

$$\begin{aligned}\Pi_{11}(\xi(k)) &= \frac{1}{1 + e^{-(\rho_{1,1}\xi(k)-1)(d_{1,1}+\rho_{1,1}\xi(k)^2)}}, \\ \Pi_{22}(\xi(k)) &= \frac{1}{1 + e^{-(\rho_{2,1}\xi(k)-1)(d_{2,1}+\rho_{2,1}\xi(k)^2)}} \\ &\quad - \frac{1}{1 + e^{-(\rho_{2,2}\xi(k)-1)(d_{2,2}+\rho_{2,2}\xi(k)^2)}}, \\ \Pi_{33}(\xi(k)) &= \frac{1}{1 + e^{-(\rho_{3,1}\xi(k)-1)(d_{3,1}+\rho_{3,1}\xi(k)^2)}} \\ &\quad - \frac{1}{1 + e^{-(\rho_{3,2}\xi(k)-1)(d_{3,2}+\rho_{3,2}\xi(k)^2)}}, \\ \Pi_{44}(\xi(k)) &= \frac{1}{1 + e^{-(\rho_{4,1}\xi(k)-1)(d_{4,1}+\rho_{4,1}\xi(k)^2)}},\end{aligned} \quad (17)$$

being $d_{s,1}$, $d_{s,2}$, $\rho_{s,1}$ and $\rho_{s,2}$ ($s \in \{1, \dots, 4\}$) some parameters whose values have been properly tuned according to the vehicle under test (see Table 1). Specifically, these parameters have been properly chosen for setting up the ranges of $\xi(k)$ for which the probabilities $\Pi_{qb}(\xi(k))$ suggest a proper transition between the modes of the IMM.

The other off-diagonal probabilities in (16) are instead defined as:

$$\Pi_{qb}(\xi(k)) = \frac{1 - \Pi_{qq}(\xi(k))}{3}, \quad (18)$$

being $q, b \in \{1, \dots, 4\}$ with $q \neq b$.

4. Co-simulation platform for virtual testing

The assessment of the VSA estimation accuracy is performed via the high-fidelity co-simulation platform embedding the dSPACE software ASM depicted in Fig. 5. It involves a full vehicle (that can be properly characterized), roads, manoeuvre, and driver models. Indeed, these are strictly needed to predict the movements of a specific vehicle on a particular road in response to both control and disturbance inputs. Accordingly, the simulation platform is composed of four layers, i.e. (i) driver layer; (ii) vehicle layer; (iii) environment layer; (iv) component-under-test layer. The driver layer consists of models essential to perform manoeuvre, i.e. predefined sequences of driving instructions for simulating a variety of driving scenarios. It handles the accelerator and brake pedals and steering in such a way that the vehicle follows a given reference velocity while driving on an arbitrary road. The task of controlling the vehicle is split into sub-tasks devoted to longitudinal control (Kiencke & Nielsen, 2005), lateral control (MacAdam, 1981), and the reference generator needed for path and velocity planning to be tracked while driving on roads (Kiencke & Nielsen, 2005). Accordingly, suitable control commands are provided to the lower vehicle layer so to command the powertrain system, i.e. propulsion and steering system. The vehicle layer considers a detailed full vehicle model emulating

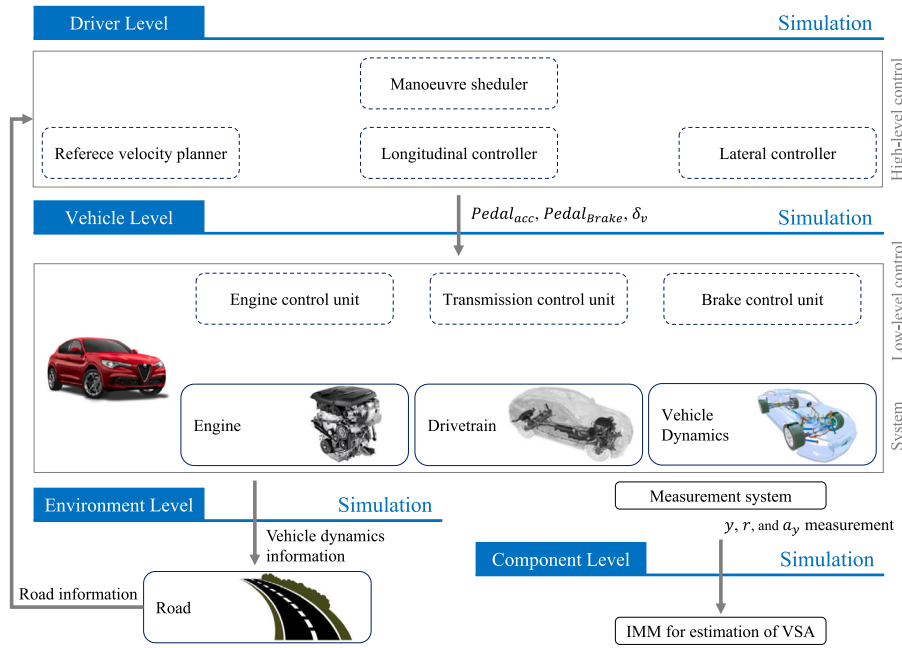


Fig. 5. High-fidelity vehicle simulation environment.

Table 2
Segment-D SUV vehicle parameters (Zal, 2023).

Quantity	Value	Quantity	Value
Mass m [kg]	1788	Height of the centre of mass [m]	0.6
Front semi-wheelbase a_1 [m]	1.35	Rear semi-wheelbase a_2 [m]	1.47
Front track width [m]	1.61	Rear track width [m]	1.64
Yaw moment of inertia J_z [kg m ²]	3230	Weight distribution [-]	50/50
Longitudinal aerodynamics drag coefficient [-]	0.32	Frontal area [m ²]	2.75
Tyre code	235/65 R 17 104 W	Steering ratio [deg/m]	5625
Max. power [kW] @ speed [rpm]	154 @ 3750	Max. torque [N m] @ speed [rpm]	470 @ 1750

all its components, such as engine, drivetrain, and vehicle dynamics, which all come together with component-level control models (Soft Electronic Control Units - ECUs) to mimic the car and its equipment. In particular, vehicle dynamics has been modelled with a Multi-body approach: the vehicle is composed of 5 bodies (15-DOF), vehicle and four wheels, including suspension kinematics and forces, tyre-road contact forces, and torques (MF-tyre 6.1), aerodynamics, steering, and brakes. The developed full vehicle model concerns a segment-D compact crossover SUV, equipped with a 2.2 L Inline-4 Multijet II 154 kW engine, a 8-speed automatic transmission with torque converter, a double wishbones suspension in the front axle, and a multi-link suspension in the rear axle. The main parameters of the vehicle are reported in Table 2 (Zal, 2023). For the IMM operation, we assume that the vehicle is equipped with GPS, IMU and all those in-vehicle sensors necessary to get the lateral position, the yaw rate, and the lateral acceleration measurement. Finally, the environment layer provides information about the road. Roads are described in terms of horizontal and vertical profile, surface conditions, modelled as junctions and road elements and their conditions. Different maps can be loaded, so to generate a specific road network and driving scenarios. The properties of the road are modelled as a function of the position of the vehicle. Therefore, the road model first calculates the longitudinal CP_x and lateral CP_y positions of the tyre contact point, and, then, the following variables at the tyre-road contact point are evaluated:

- road height $CP_z = f(CP_x, CP_y)$;
- normal unit vector of road $e_{zCP} = f(CP_x, CP_y)$;
- road friction coefficient $c_{f,CP} = f(CP_x, CP_y)$.

4.1. Parameter setting

The IMM algorithm consists of an array of parallel filters properly parameterized to represent the handling dynamics behaviour of the vehicle in four different road surface conditions, i.e. dry, damp, wet, and snowy asphalt. To this aim, the parameters of the four prediction models have been properly tuned by leveraging data from the co-simulation platform that embeds the detailed dSPACE software ASM of the vehicle of interest. For each of them, front and rear axle characteristics were carried out on the Segment-D-SUV vehicle model, including the effects of several set-up parameters, like camber angles and roll steer angles (Guiggiani, 2014). The Dugoff's model parameters, $c_{f,max}$ and C_{a_i} in (5), (7) and (8) have been evaluated to reconstruct the front and rear axle characteristics (see Table 3).

The look-up table needed to compute the actual value of the reference lateral acceleration $a_{y_k}^{Dry}$ has been properly obtained via a common procedure detailed in Guiggiani (2014) and is based on a set of step-steer manoeuvres (Russo, Russo, & Volpe, 2000) useful to investigation of the vehicle's lateral dynamics in dry conditions. To this purpose, a wide range of manoeuvre should be performed for different value of the steering angle δ_v and the forward speed v_x , and then the steady-state lateral acceleration $a_{y_k}^{Dry}$, as well as the corresponding manoeuvre inputs δ_v and v_x , have to be stored. Since the complete coverage of all the different conditions requires a huge number of manoeuvres, it can consume a large amount of time and resources, so here we have reduced the number of characteristic points to be evaluated following the approach in Panáček, Semela, Adamec, and Schüllerová (2016) where

the following two-dimensional analytical relationship is exploited:

$$\begin{aligned} a_y^{Dry} = & a_y^{Dry}(\delta_{v,0}, v_{x,0}) + \rho_{\delta_v} \delta_{v_n} + \phi_{\delta_v} \delta_{v_n}^2 + \epsilon_{\delta_v} \delta_{v_n}^3 \\ & + \rho_{v_x} v_{x_n} + \phi_{v_x} v_{x_n}^2 + \epsilon_{v_x} v_{x_n}^3 + \varsigma_1 \delta_{v_n} v_{x_n} \\ & + \varsigma_2 \delta_{v_n} v_{x_n}^2 + \varsigma_3 \delta_{v_n}^2 v_{x_n} + \varsigma_4 \delta_{v_n}^2 v_{x_n}^2, \end{aligned} \quad (19)$$

with δ_{v_n} and v_{x_n} defined as:

$$\delta_{v_n} = \frac{2\delta_v}{\Delta\delta_v} - 1, \quad v_{x_n} = \frac{2v_x}{\Delta v_x} - 1, \quad (20)$$

where, $\Delta\delta_v$ and Δv_x are the exploitable inputs ranges of the steering angle δ_v and vehicle speed v_x , respectively. See Fig. 6 for the typical 3-dimensional surface reconstructed via the relationship (19).

The parameters in (19), i.e., ρ_{δ_v} , ϕ_{δ_v} , ϵ_{δ_v} , ρ_{v_x} , ϕ_{v_x} , ϵ_{v_x} , ς_1 , ς_2 , ς_3 and ς_4 , can be evaluated by just considering 11 representative manoeuvres with inputs $\delta_{v,\zeta}$ and $v_{x,i}$, where $\zeta, i \in \{B, 0, T\}$ identify bottom (B), middle (0) and top (T) values of exploitable ranges $\Delta\delta_v$ and Δv_x , respectively. Now, 9 of the required manoeuvres are executed to evaluate the reference lateral acceleration setting inputs at bottom (B), middle (0) and top (T) values of steering angle and vehicle speed exploitable ranges ($a_y^{Dry}(\delta_{v,T}, v_{x,T})$, $a_y^{Dry}(\delta_{v,T}, v_{x,B})$, $a_y^{Dry}(\delta_{v,B}, v_{x,B})$, $a_y^{Dry}(\delta_{v,B}, v_{x,T})$, $a_y^{Dry}(\delta_{v,0}, v_{x,T})$, $a_y^{Dry}(\delta_{v,0}, v_{x,B})$, $a_y^{Dry}(\delta_{v,0}, v_{x,0})$, $a_y^{Dry}(\delta_{v,B}, v_{x,0})$, $a_y^{Dry}(\delta_{v,0}, v_{x,0})$), while the remaining 2 manoeuvres are executed to assess lateral acceleration increments with the steering angle $\partial a_y^{Dry}(\delta_{v,0}, v_{x,0})/\partial\delta_v$, and vehicle speed $\partial a_y^{Dry}(\delta_{v,0}, v_{x,0})/\partial v_x$ at the look-up table intermediate point $a_y^{Dry}(\delta_{v,0}, v_{x,0})$ (see also Fig. 6).

Once obtained these lateral acceleration values, the overall look-up table (surface) can be reconstructed over the entire input ranges by computing the parameters in (19) as:

$$\begin{aligned} \rho_{\delta_v} &= \frac{\partial a_y^{Dry}(\delta_{v,0}, v_{x,0})}{\partial\delta_v} \frac{\Delta\delta_v}{2}, \\ \phi_{\delta_v} &= (\Delta a_{y,T0}^{Dry} + \Delta a_{y,B0}^{Dry})/2, \\ \epsilon_{\delta_v} &= -\rho_{\delta_v} + (\Delta a_{y,T0}^{Dry} - \Delta a_{y,B0}^{Dry})/2, \\ \rho_{v_x} &= \frac{\partial a_y^{Dry}(\delta_{v,0}, v_{x,0})}{\partial v_x} \frac{\Delta v_x}{2}, \\ \phi_{v_x} &= (\Delta a_{y,0T}^{Dry} + \Delta a_{y,0B}^{Dry})/2, \end{aligned} \quad (21)$$

$$\begin{aligned} \epsilon_{v_x} &= -\rho_{v_x} + (\Delta a_{y,0T}^{Dry} - \Delta a_{y,0B}^{Dry})/2, \\ \varsigma_1 &= (\Gamma_{TT} - \Gamma_{TB} - \Gamma_{BT} + \Gamma_{BB})/4, \\ \varsigma_2 &= (\Gamma_{TT} + \Gamma_{TB} - \Gamma_{BT} - \Gamma_{BB})/4, \\ \varsigma_3 &= (\Gamma_{TT} - \Gamma_{TB} + \Gamma_{BT} - \Gamma_{BB})/4, \\ \varsigma_4 &= (\Gamma_{TT} + \Gamma_{TB} + \Gamma_{BT} + \Gamma_{BB})/4, \end{aligned}$$

with,

$$\begin{aligned} \Gamma_{TT} &= \Delta a_{y,TT}^{Dry} - (\Delta a_{y,0T}^{Dry} + \Delta a_{y,T0}^{Dry}), \\ \Gamma_{TB} &= \Delta a_{y,TB}^{Dry} - (\Delta a_{y,0B}^{Dry} + \Delta a_{y,T0}^{Dry}), \\ \Gamma_{BT} &= \Delta a_{y,BT}^{Dry} - (\Delta a_{y,0T}^{Dry} + \Delta a_{y,B0}^{Dry}), \\ \Gamma_{BB} &= \Delta a_{y,BB}^{Dry} - (\Delta a_{y,0B}^{Dry} + \Delta a_{y,B0}^{Dry}), \\ \Delta a_{y,TT}^{Dry} &= a_y^{Dry}(\delta_{v,T}, v_{x,T}) - a_y^{Dry}(\delta_{v,0}, v_{x,0}), \\ \Delta a_{y,TB}^{Dry} &= a_y^{Dry}(\delta_{v,T}, v_{x,B}) - a_y^{Dry}(\delta_{v,0}, v_{x,0}), \\ \Delta a_{y,BT}^{Dry} &= a_y^{Dry}(\delta_{v,B}, v_{x,T}) - a_y^{Dry}(\delta_{v,0}, v_{x,0}), \\ \Delta a_{y,BB}^{Dry} &= a_y^{Dry}(\delta_{v,B}, v_{x,B}) - a_y^{Dry}(\delta_{v,0}, v_{x,0}), \\ \Delta a_{y,0T}^{Dry} &= a_y^{Dry}(\delta_{v,0}, v_{x,T}) - a_y^{Dry}(\delta_{v,0}, v_{x,0}), \\ \Delta a_{y,T0}^{Dry} &= a_y^{Dry}(\delta_{v,T}, v_{x,0}) - a_y^{Dry}(\delta_{v,0}, v_{x,0}), \\ \Delta a_{y,0B}^{Dry} &= a_y^{Dry}(\delta_{v,0}, v_{x,B}) - a_y^{Dry}(\delta_{v,0}, v_{x,0}), \\ \Delta a_{y,B0}^{Dry} &= a_y^{Dry}(\delta_{v,B}, v_{x,0}) - a_y^{Dry}(\delta_{v,0}, v_{x,0}). \end{aligned} \quad (22)$$

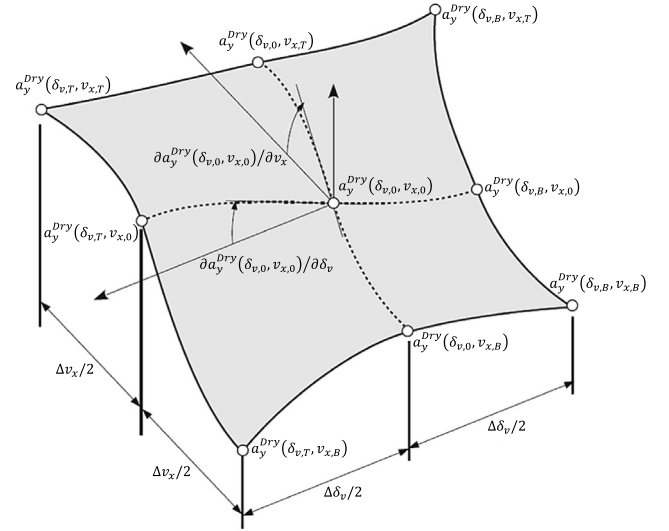


Fig. 6. Reference lateral acceleration of the vehicle under dry road surface condition, a_y^{Dry} .

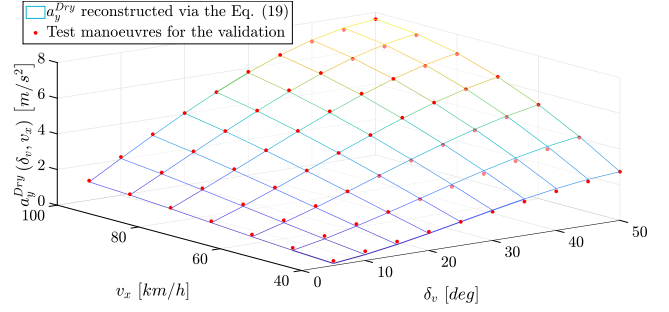


Fig. 7. Reference lateral acceleration in dry asphalt condition a_y^{Dry} for the considered Segment-D SUV vehicle.

The above procedure has been hence applied to our Segment-D SUV vehicle. In doing so, the following vehicle manoeuvre inputs ranges $v_x = 40 - 100$ [km/h] and $\delta_v = 0 - 50$ [deg] (extended to $\delta_v = -50 - 0$ [deg] for symmetry) in terms of speed and steering angle respectively, have been considered. In this case, only 8 manoeuvres are required to characterize the reference lateral acceleration of the vehicle over the entire inputs ranges, whose results are reported in Table 4, since for steering angle of zero the lateral acceleration is trivially zero. The overall look-up table (surface) is instead depicted in Fig. 7. Herein, the red dots refer to reference lateral acceleration a_y^{Dry} evaluated in 70 test manoeuvre selected for the validation. Results highlight how this approach accurately reproduces the vehicle's steady-state lateral acceleration, with a mean error over the whole set of 70 manoeuvre that does not exceed 5%.

Remark 2. It is important to highlight that the well-known adopted procedure requires performing a wide range of manoeuvres for different values of the forward vehicle's velocity v_x and the steering angle δ_v and is strictly correlated to the computational resources available. Therefore, by increasing the time and the operational effort, it is possible to extend the range of the vehicle's speed and the steering angle, as well as the sampling step of these. Furthermore, it is worth observing that the dry reference lateral acceleration values obtained via the map in Fig. 7 are referred to the tested Segment-D SUV vehicle, whose parameters are in Table 2.

Table 3
Dugoff model parameters' values in different road conditions.

Parameter	Dry road	Damp road	Wet road	Snowy road
C_{a_1} [N/deg]	2790	2790	3140	3140
C_{a_2} [N/deg]	3490	3315	3315	3140
$c_{f,max}$ [-]	1.05	0.95	0.77	0.6

Table 4

Parameters values of eq. (19) to reconstruct the reference lateral acceleration a_y^{Dry} of the Segment-D SUV vehicle in dry asphalt condition.

Parameter	Value
$a_y^{Dry}(\delta_{v,T}, v_{x,T})$ [m/s ²]	7.62
$a_y^{Dry}(\delta_{v,T}, v_{x,B})$ [m/s ²]	2.73
$a_y^{Dry}(\delta_{v,T}, v_{x,0})$ [m/s ²]	6.22
$a_y^{Dry}(\delta_{v,0}, v_{x,T})$ [m/s ²]	4.94
$a_y^{Dry}(\delta_{v,0}, v_{x,B})$ [m/s ²]	1.32
$a_y^{Dry}(\delta_{v,0}, v_{x,0})$ [m/s ²]	3.36
$\partial a_y^{Dry}(\delta_{v,0}, v_{x,0}) / \partial \delta_v$ [(m/s ²) / deg]	0.14
$\partial a_y^{Dry}(\delta_{v,0}, v_{x,0}) / \partial v_x$ [(m/s ²) / (km/h)]	0.06

5. Analysis and validation

Leveraging the co-simulation platform presented in Section 4, several driving scenarios have been executed to widely verify the effectiveness and performance of the designed methodologies. First, a Monte Carlo analysis was carried out to disclose the VSA estimation accuracy via the proposed state-dependent IMM described in the previous Section 3.1. The investigation continues with a performance comparative analysis of both the filtering Kalman-based solutions (EKF ad UKF) developed according to the design procedure. Moreover, in order to better evaluate the effect of the adaptive TPM, the performance of the state-dependent IMM has also been compared with the one achievable via a classical UKF-based IMM equipped with a constant transition probability matrix. Finally, to better highlight the advantages of the novel proposed strategy, the best IMM filter (as determined earlier) has been tested in a real driving track scenario emulated via the high-fidelity co-simulation platform embedding ASM, in order to verify the estimation efficiency in case of sudden changes in road surface conditions. All the above validation steps are detailed in the following.

5.1. Monte Carlo analysis

To evaluate the VSA estimation accuracy achieved via the proposed state-dependent IMM w.r.t. to the once achievable via a constant TPM policy, an extensive simulation campaign was carried out. Specifically, the constant TPM policy has been selected to assign the same probability to each of the 4 IMM's modes. The comparative analysis has been performed considering both UKF and EKF-based IMM solutions (IMMUKF and IMMEKF, respectively). More specifically, a Monte Carlo simulation is carried out to test the classical UKF-based IMM with constant TPM against the IMMUKF and IMMEKF with the time-variant TPM in Eqs. (16), (17) and (18) selected as in Section 3.2.

The number of iterations has been set to 100, and the initial conditions $\hat{x}_{0|0}$ were varied as a normal distribution with mean value equal to true value of the initial vehicle state x_0 , i.e., $\hat{x}_{0|0} \in \mathcal{N}(x_0, \sqrt{P_{0|0}})$. The initial covariance error matrix $P_{0|0}$ is selected in accordance with the variances of the initial conditions, as:

$$\begin{aligned} P_{0|0} &= \text{diag}(\sigma_y^2, \sigma_{v_y}^2, \sigma_\phi^2, \sigma_r^2, \sigma_{F_{y1}}^2, \sigma_{F_{y2}}^2) \\ &= \text{diag}(5^2, 0.1^2, 6^2, 1^2, (1e4)^2, (1e4)^2). \end{aligned} \quad (23)$$

The driving simulation scenario is characterized by steering pad manoeuvre. Considering the vehicle driving at constant speed v_x on a road with a constant friction coefficient $c_{f,CP}$, starting from initial vehicle state $x_0 = 0 \cdot I_{6 \times 1}$, the control command δ_v (steering angle) is given to the vehicle at time step $k = 0$ [s], and keeping it constant for 10 [s]. The

Table 5

Steering pad manoeuvre: scenario parameters range.

Parameter	Range
δ_v [deg]	$\pm(30\text{--}50)$
v_x [km/h]	80–100
$c_{f,CP}$ [-]	0.6–1

manoeuvre' parameters (i.e. δ_v , v_x and $c_{f,CP}$) have been made to vary following the Monte Carlo approach as random variables with uniform distribution within the ranges reported in the Table 5.

The process noise covariance matrix Q is the same for the three filters:

$$Q = \begin{bmatrix} \psi_1 \frac{\Delta t^3}{3} & \psi_1 \frac{\Delta t^2}{2} & 0 & 0 & 0 & 0 \\ \psi_1 \frac{\Delta t^2}{2} & \psi_1 \Delta t & 0 & 0 & 0 & 0 \\ 0 & 0 & \psi_2 \frac{\Delta t^3}{3} & \psi_2 \frac{\Delta t^2}{2} & 0 & 0 \\ 0 & 0 & \psi_2 \frac{\Delta t^2}{2} & \psi_2 \Delta t & 0 & 0 \\ 0 & 0 & 0 & 0 & \psi_3 \Delta t & 0 \\ 0 & 0 & 0 & 0 & 0 & \psi_4 \Delta t \end{bmatrix} \quad (24)$$

where ψ_1 – ψ_4 are tuning parameters, and the measurement noise covariance matrix is set to be

$$R = \text{diag}(\sigma_y, \sigma_r, \sigma_{a_y}) = \text{diag}(5, 1, 0.1). \quad (25)$$

The Monte Carlo analysis is summarized in Figs. 8–13, where the results have been carefully post-processed to clearly represent the uncertainty of the estimation algorithms in terms of:

- mean estimation error \bar{e}_k obtained on N Monte Carlo samples (red line). For each k th time step, the following performance index is evaluated:

$$\bar{e}_k = \frac{1}{N} \sum_{\chi=1}^N (x_{k,\chi} - \hat{x}_{k,\chi}); \quad (26)$$

- standard deviation of the estimation errors obtained on N Monte Carlo samples (dashed blue line), evaluated for each k th time step as:

$$\sigma_k = \sqrt{\frac{1}{N-1} \sum_{\chi=1}^N |(x_{k,\chi} - \hat{x}_{k,\chi}) - \bar{e}_k|^2}; \quad (27)$$

- estimation error of a single Monte Carlo sample (green line).

Fig. 8(a), (b), and (c) show estimation errors of the lateral velocity v_y (and, therefore, of the VSA) among the classical IMMUKF with constant TPM, state-dependent IMMUKF and state-dependent IMMEKF, respectively. The results reveal that both the proposed IMMUKF and IMMEKF with state-dependent TPM provides more consistent results than the classical approach with constant TPM. Indeed, the standard deviation of the estimation errors on N Monte Carlo samples (dashed blue line) obtained with both the two state-dependent algorithms converge to 0.035 [m/s] after 10 [s], much lower than 0.13 [m/s] of the classical IMMUKF. The green lines in these figures are the estimation errors of a single Monte Carlo sample, selected among the N samples to highlight the maximum VSA estimation error. Specifically, it refers to the following simulation scenario: $\hat{x}_{0|0} = [2.1, -0.03, 7.68, 1.39, -5028, -11164]^T$, $\delta_v = -35.70$ [deg], $v_x = 91.30$ [km/h] and $c_{f,CP} = 0.92$ [-]. The estimation

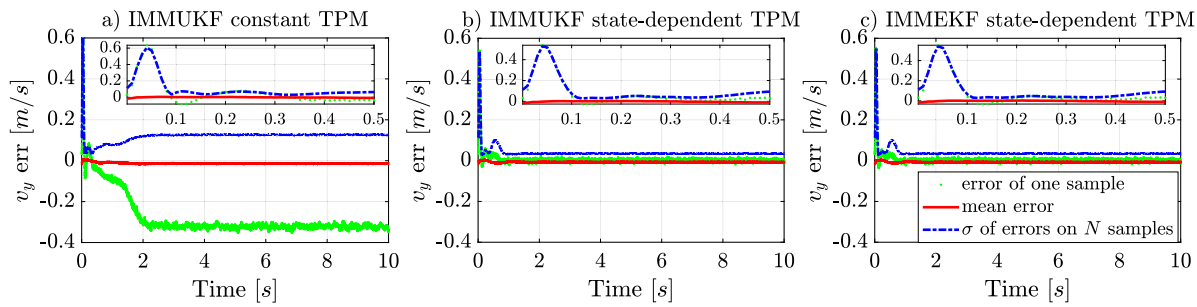


Fig. 8. Time histories of estimation errors of the lateral velocity v_y among: (a) the classical IMMUKF with constant TPM; (b) the proposed IMMUKF with state-dependent TPM; (c) the proposed IMMEKF with state-dependent TPM. (For interpretation of the references to colour in this figure legend, the reader is referred to the web version of this article.)

Table 6

IMMUKF with constant TPM: σ of the estimation errors on N samples.

Quantity	σ	Quantity	σ
v_y [m/s]	0.13	y [m]	0.21
φ [deg]	1.46	r [deg/s]	0.74
F_{y_1} [N]	931	F_{y_2} [N]	1097

error of the IMMUKF with constant TPM converges to -0.33 [m/s], which exhibits, therefore, poor estimation properties with respect to tyre-road friction coefficient variations, mainly due to a wrong mode probability update. Indeed, the relative estimation error of VSA β , defined as $|(\hat{\beta} - \beta)/\beta|$, after 10 [s] results to be of 98%. In the same scenario, both the state-dependent IMMUKF and IMMEKF successfully estimate the VSA, with a relative error of 1% after 10 [s], confirming the need to adopt the proposed approach to deal with tyre-road friction coefficient variations.

Concerning the other state variables, all the three analysed solutions give a successful estimation. Indeed, Fig. 9 to 13 shows that: the estimation error means (red lines) are bounded around the zero value, as it should be when all available information is utilized correctly; the standard deviation of the estimation errors on N Monte Carlo samples (dashed blue line) converge to the true value, indicating a discrete observability of the system; the estimation error of the single run of the Monte Carlo simulation (green lines) remain within the bounds defined by the dashed blue line for at least 66% of the simulation time. Minor improvements in the estimation of these quantities have been achieved via the state-dependent IMMUKF and IMMEKF, that can be drawn by particularly analysing Fig. 14, where the standard deviation trends of the estimation errors for the three methodologies are compared. Except for lateral position estimation (14(a)), that shows good agreement with true value via all the three analysed solutions (see 14(a)), the estimation errors of φ , r , F_{y_1} and F_{y_2} with the state-dependent IMMUKF and IMMEKF converge to lower values than classical IMMUKF (see 14(c)–(d)). Note that, this can be clearly appreciated by comparing the σ computed after 10 [s]. The comparative results are also reported in Tables 6–8 for ease of readability.

Finally, when directly comparing IMMUKF and IMMEKF, no significant deviations have been evaluated, highlighting how the two approaches exhibit the same estimation properties. However, the state-dependent IMMUKF result is the most accurate in the estimation of the yaw rate and tyres lateral force, which demonstrates the strength of adopting an UKF-based solution over an EKF one, especially when strong driving nonlinearities occur and the first-order linearization of the EKF algorithm in the Jacobian matrix becomes too significant. Indeed, acting directly on the nonlinear model via the state approximation performed by using a set of sigma points typical of the unscented transformation, the estimation performance of the IMMUKF turns out to be superior.

Table 7

IMMUKF with state-dependent TPM: σ of the estimation errors on N samples.

Quantity	σ	Quantity	σ
v_y [m/s]	0.04	y [m]	0.21
φ [deg]	1.32	r [deg/s]	0.40
F_{y_1} [N]	878	F_{y_2} [N]	745

Table 8

IMMEKF with state-dependent TPM: σ of the estimation errors on N samples.

Quantity	σ	Quantity	σ
v_y [m/s]	0.04	y [m]	0.21
φ [deg]	1.32	r [deg/s]	0.43
F_{y_1} [N]	898	F_{y_2} [N]	780

Table 9

Steer ramp and double-lane change manoeuvres: scenario parameters range.

Parameter	Range
v_x [km/h]	40–100
$\partial\delta_v/\partial t$ [deg/s]	$\pm(50-250)$
δ_v [deg]	$\pm(10-50)$
$c_{f,CP,1}$ [–]	0.5–1
$c_{f,CP,2}$ [–]	0.5–1

5.2. Manoeuvres performance analysis

In this section, we further corroborate the effectiveness of the proposed approach leveraging a set of typical ramp steer and double-lane change manoeuvres, commonly applied to assess the handling and performance characteristics of road vehicles (Demerly & Youcef-Toumi, 2000). For generating synthetic data, the high-fidelity co-simulation platform outlined in Section 4 has been used, with steering angle and reference speed as inputs. The ramp steer manoeuvres involve a gradual and continuous increment in steering angle with a constant rate. Specifically, the vehicle begins travelling in a straight line at a constant speed v_x , and then, at 2.5 [s], the steering angle increases at a steady and constant rate $\partial\delta_v/\partial t$. At the 8.0 [s] a sudden change in road surface occurs and the friction coefficient passes from $c_{f,CP,1}$ to $c_{f,CP,2}$, signalling the completion of the manoeuvres at 10 [s]. Regarding the double-lane change manoeuvre, instead, it is employed to replicate emergency scenarios that need rapid evasive actions to circumvent unforeseen obstacles, followed by a swift return to the initial lane. In detail, the vehicle proceeds in a straight line at a specified speed v_x until the 2.0 [s] mark. After, a prompt steering action is performed to reach a δ_v angle, in order to mimic a lateral shift to an adjacent lane. Subsequently, a second steering manoeuvre happens to realign the vehicle back into the original lane. A notable variation in the road surface conditions is encountered at 3.4 [s], where the friction coefficient transitions from $c_{f,CP,1}$ to $c_{f,CP,2}$, and the procedure concludes at 6.0 [s].

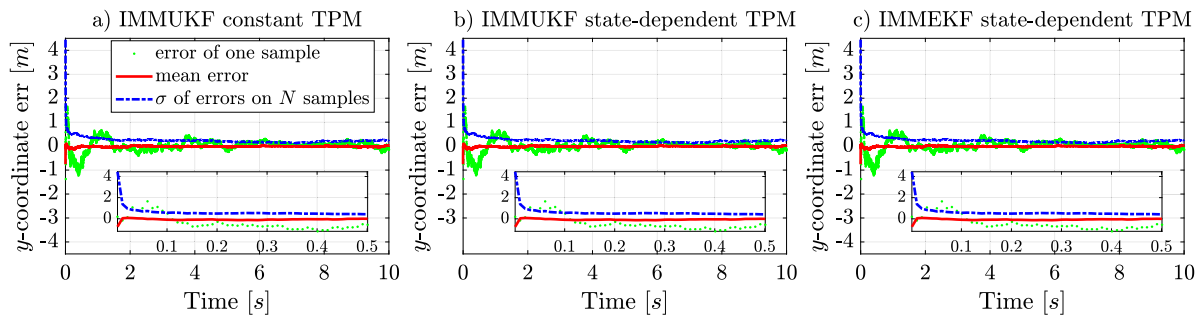


Fig. 9. Time histories of estimation errors of y-coordinate among: (a) the classical IMMUKF with constant TPM; (b) the proposed IMMUKF with state-dependent TPM; (c) the proposed IMMEKF with state-dependent TPM. (For interpretation of the references to colour in this figure legend, the reader is referred to the web version of this article.)

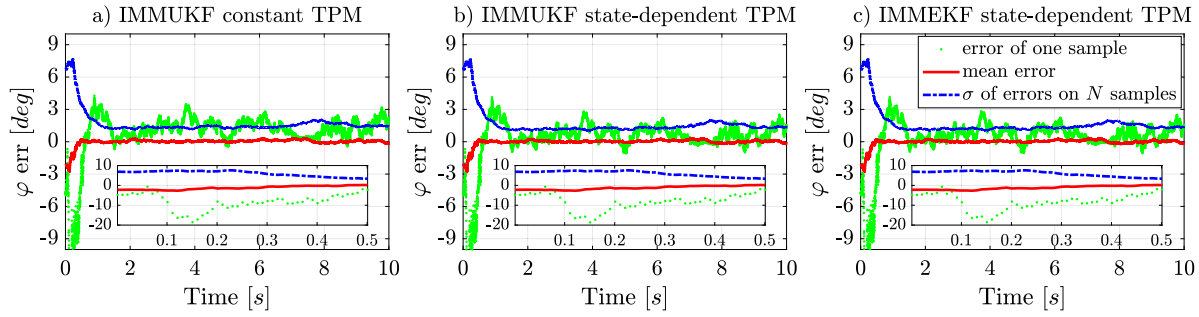


Fig. 10. Time histories of estimation errors of the yaw angle φ among: (a) the classical IMMUKF with constant TPM; (b) the proposed IMMUKF with state-dependent TPM; (c) the proposed IMMEKF with state-dependent TPM. (For interpretation of the references to colour in this figure legend, the reader is referred to the web version of this article.)

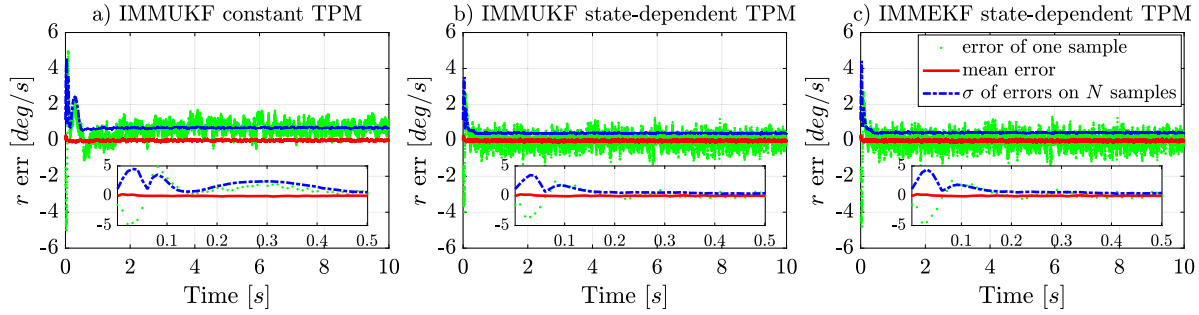


Fig. 11. Time histories of estimation errors of the yaw rate r among: (a) the classical IMMUKF with constant TPM; (b) the proposed IMMUKF with state-dependent TPM; (c) the proposed IMMEKF with state-dependent TPM. (For interpretation of the references to colour in this figure legend, the reader is referred to the web version of this article.)

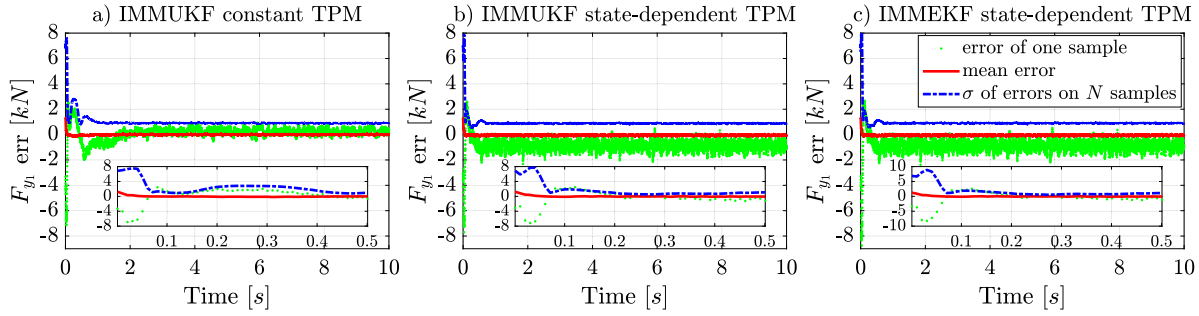


Fig. 12. Time histories of estimation errors of the front lateral tyre force F_{yi} among: (a) the classical IMMUKF with constant TPM; (b) the proposed IMMUKF with state-dependent TPM; (c) the proposed IMMEKF with state-dependent TPM. (For interpretation of the references to colour in this figure legend, the reader is referred to the web version of this article.)

To verify the performance of our algorithm, we compare its skills in estimating the sideslip angle β with respect to a classical IMM whose update mode is based on a constant TPM and two Kalman filter solutions, i.e. EKF and UKF. More specifically, for both of the examined scenarios (the ramp steer and the double-lane change) we

conducted $N = 100$ Monte Carlo simulations to evaluate each of the aforementioned estimation methods. The initial vehicle state x_0 , the initial conditions $\hat{x}_{0|0}$, and the initial covariance error matrix $P_{0|0}$ were selected based on the parameters established in the prior Monte Carlo simulation detailed in Section 5.1. Furthermore, the parameters for

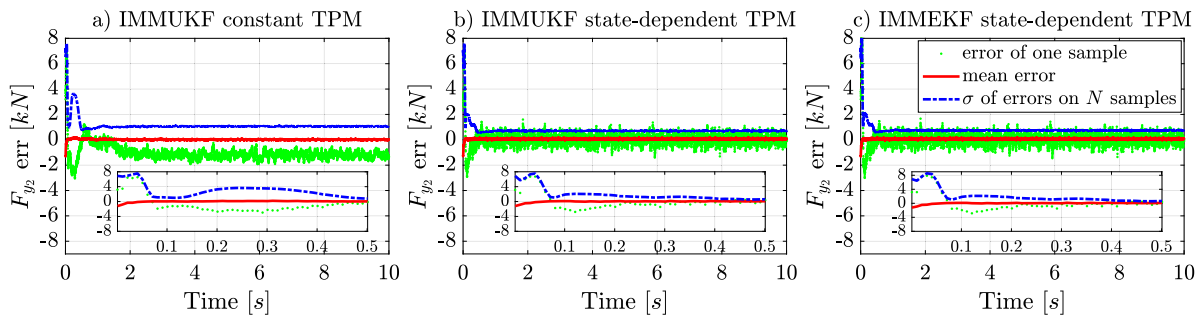


Fig. 13. Time histories of estimation errors of the rear lateral tyre force F_{y_2} among: (a) the classical IMMUKF with constant TPM; (b) the proposed IMMUKF with state-dependent TPM; (c) the proposed IMMEKF with state-dependent TPM. (For interpretation of the references to colour in this figure legend, the reader is referred to the web version of this article.)

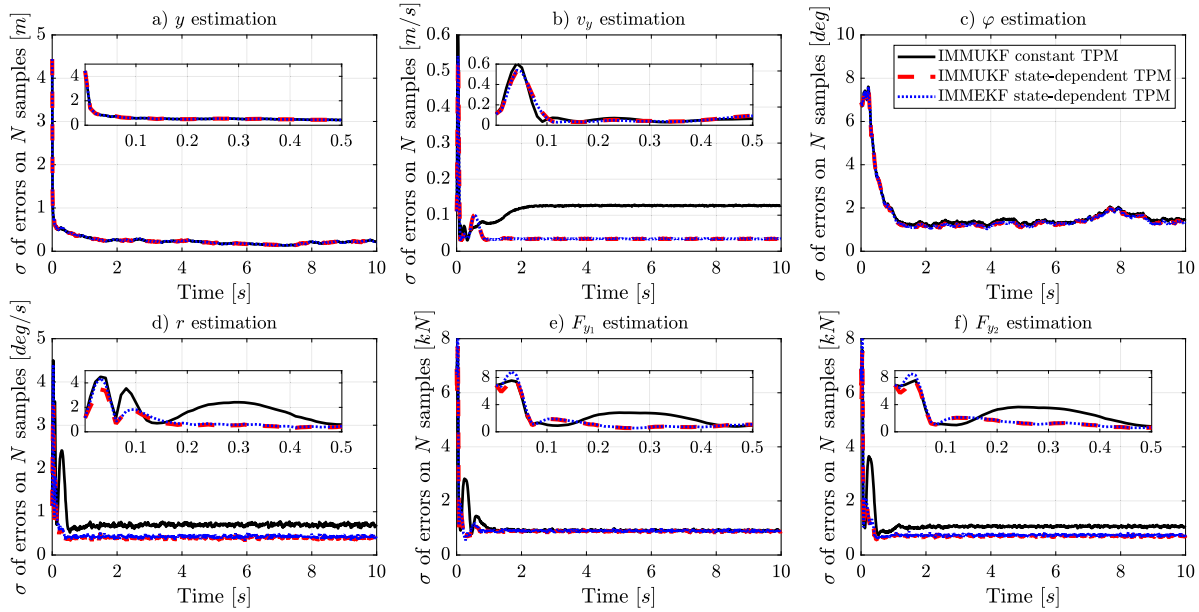


Fig. 14. Time histories of standard deviation of the estimation errors in a comparative analysis among a classical IMMUKF with constant TPM (dashed black lines), the proposed IMMUKF with a state-dependent TPM (dashed red lines) and the proposed IMMEKF with a state-dependent TPM (dashed blue lines) for: (a) y estimation; (b) v_y estimation; (c) φ estimation; (d) r estimation; (e) F_{y_1} estimation; (f) F_{y_2} estimation. (For interpretation of the references to colour in this figure legend, the reader is referred to the web version of this article.)

both the ramp steer and double-lane change manoeuvres, as well as the road surface conditions, (i.e. v_x , $\partial\delta_v/\partial t$, δ_v , $c_{f,CP,1}$ and $c_{f,CP,2}$) were varied in accordance with the Monte Carlo method and were emulated as random variables with a uniform distribution within the range specified in Table 9. Thus, the Root Mean Square Error (RMSE) index (Lee & Park, 2022) is exploited on N realization to compare the estimation accuracy. Simulation results can be observe in Figs. 15–16 for the two aforementioned manoeuvres, where it is easily to verify how the estimation errors of the proposed state-dependent IMM solution are smaller than those of the traditional solutions, i.e. the IMM with a constant TPM and the EKF and UKF Kalman filters. Specifically, Fig. 15 illustrates the RMSE pertaining to the estimation of sideslip angles during ramp steer manoeuvres throughout the complete Monte Carlo trial. All the analysed algorithms start with an initial RMSE of 0.4 [deg] and quickly converge to a value close to zero. At 2.5 [s], the vehicle begins steering. It is worth highlighting that all the analysis algorithms exhibit a progressive increase in the RMSE when estimating the sideslip angle over time. This behaviour can be attributed to the nature of the ramp steering manoeuvre. As the steering angle steadily increases with time, it is well-known that high steering angles correspond to a heightened likelihood of the tyre slip angles approaching the nonlinear region of the tyre's characteristics. Under these conditions, the accuracy of the dynamic equation in the single-track model decreases, leading to

a subsequent rise in process noise. After 6 s of simulation, the RMSE for the IMMUKF with constant TPM deviates to higher values due to inaccuracies in the evaluation of the likelihood functions and the probability updates as well, indicating poor robustness. Notably, the RMSE values for the IMMEKF with constant TPM, UKF and EKF are higher than those of the proposed approach with state-dependent TPM. To assess the estimation algorithms' ability to handle sudden changes in road surface conditions, a scenario involving two different friction coefficients is considered. At the 8 s mark, a sudden shift in road surface conditions occurs, with the road surface being randomly selected among dry, damp, wet, and snowy conditions using the Monte Carlo approach. After this transitioning, both the IMMUKF and IMMEKF with a constant TPM exhibit unsuccessful performance in estimating the sideslip angle. This issue points out mainly due to poor estimation in some realizations where the vehicle is performing demanding manoeuvres. The use of a constant TPM in such situations leads to the evaluation of likelihood functions that incorrectly assign higher probabilities to low friction modes, specifically, modes s_3 (indicative of wet asphalt) and s_4 (indicative of snowy asphalt), even if the vehicle is driving on dry asphalt. It is worth noting that when the vehicle is travelling on a road with a greater friction coefficient, it may engage in manoeuvres that cause the vehicle's axle characteristics to exceed their maximum values. These maximum values align with the available

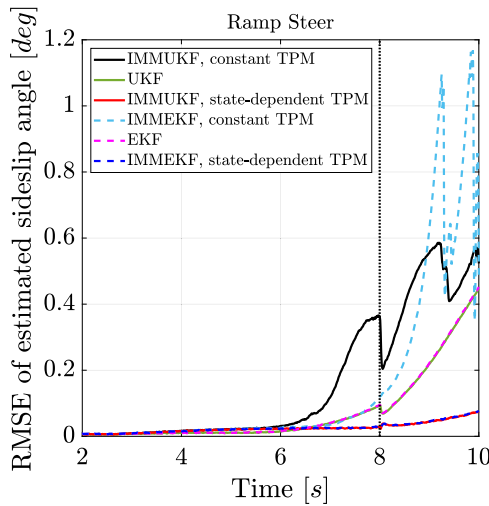


Fig. 15. Time histories of RMSE of the sideslip angle estimation in a comparative analysis among an IMMUKF with constant TPM (black lines), a UKF (green lines), the proposed IMMUKF with a state-dependent TPM (red lines), an IMMEKF with constant TPM (dashed cyan lines), a EKF (dashed magenta lines), and the proposed IMMEKF with a state-dependent TPM (dashed blue lines) for ramp steer manoeuvres with sudden changes in road surface at 8.0 [s]. (For interpretation of the references to colour in this figure legend, the reader is referred to the web version of this article.)

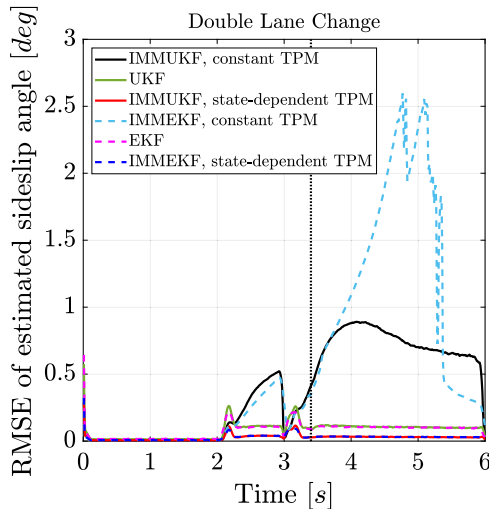


Fig. 16. Time histories of RMSE of the sideslip angle estimation in a comparative analysis among an IMMUKF with constant TPM (black lines), a UKF (green lines), the proposed IMMUKF with a state-dependent TPM (red lines), an IMMEKF with constant TPM (dashed cyan lines), a EKF (dashed magenta lines), and the proposed IMMEKF with a state-dependent TPM (dashed blue lines) for double-lane change manoeuvres with sudden changes in road surface at 3.4 [s]. (For interpretation of the references to colour in this figure legend, the reader is referred to the web version of this article.)

lateral grip on wet and snowy road surfaces. In such scenarios, the grip limit, as defined by the Dugoff tyre model for wet and snowy asphalt, is exceeded. This, in turn, renders the single-track vehicle model unstable. The consequences of this instability have a detrimental effect on the accuracy of sideslip angle estimation. Notably, both the state-dependent IMMUKF and IMMEKF demonstrate enhancements in the estimation performance, since the RMSE within 10 [s] of simulation is observed to be 0.075 [deg] for both of the proposed solutions, while with the other analysed algorithm the RMSE are up to 0.4 [deg].

Regarding the double-lane change manoeuvre, Fig. 16 presents a comprehensive depiction of the RMSE associated with the estimation of sideslip angles across the entire Monte Carlo trial. Similarly to the observations made during the analysis of ramp steer manoeuvre results,

all examined algorithms starting from an initial value of RMSE swiftly converging to a near-zero values. At 2 s, an abrupt steering action is executed to transition to an adjacent lane. In this instance, the RMSE for the IMMs with a constant TPM, along with the UKF and EKF, manifests a deviation towards higher values, thereby underscoring their suboptimal estimation performance during demanding and non-stationary driving manoeuvres. Following the lane change, a second steering manoeuvre is executed to return the vehicle to its original lane. Consistent with the approach used for the ramp steer manoeuvre, the double-lane change scenario takes into account two distinct friction coefficients. At the 3.4 s mark, there is an abrupt transition in road surface conditions, with the road surface condition being stochastically selected among dry, damp, wet, and snowy conditions through the Monte Carlo approach. Here too, after the friction coefficient transitioning, the RMSE for both IMMUKF and IMMEKF with constant TPM unstably diverges due to inaccuracies in mode probability updates as prior described, indicating poor robustness. Of particular significance is the enhanced estimation performance observed in both the state-dependent IMMUKF and IMMEKF. In this case, the RMSE results to be 0.04 [deg] at 6 s of simulation, lower with respect to the UKF and EKF.

Fig. 17(a)–(f) depict the sideslip angle estimations in a comprehensive comparative analysis among an IMMUKF with constant TPM (black lines), a UKF (green lines), the proposed IMMUKF with a state-dependent TPM (red lines), an IMMEKF with constant TPM (dashed cyan lines), a EKF (dashed magenta lines), and the proposed IMMEKF with a state-dependent TPM (dashed blue lines). These sideslip angle estimations are obtained in six specific realizations: (a) ramp steer manoeuvre with a change from wet to dry in road surface; (b) ramp steer manoeuvre with a change from snowy to dry in road surface; (c) ramp steer manoeuvre with a change from snowy to wet in road surface; (d) Double-lane change with a change from wet to dry in road surface; (e) Double-lane change with a change from snowy to dry in road surface; (f) Double-lane change with a change from snowy to wet in road surface. These six realizations have been selected to emphasize the limitations of the classical IMM approach with a constant TPM, as well as the shortcomings of both the UKF and EKF, particularly under challenging driving conditions. In contrast, the proposed approach demonstrates its ability to effectively estimate sideslip angles under such demanding conditions.

Continuing from the previously discussed analyses, we delve into the results derived from a series of further simulations aimed at assessing the efficacy of the proposed IMMEKF/IMMUKF with a state-dependent TPM for the estimation of the vehicle sideslip angle. This method's performance is evaluated against a spectrum of existing algorithms in the domain, encompassing deep learning-based methods (Ghosh, Tonoli, & Amati, 2018; Kim, Min, Kim, & Huh, 2020), model-based approaches (You, Hahn, & Lee, 2009), and deep ensemble-based adaptive EKF/UKF estimators (Kim et al., 2020). The assessment utilized an array of five simulation scenarios reported in Table 10, each characterized by different and challenging driving conditions. Specifically, they included a double lane change on both dry asphalt and snow-covered roads at a speed of 120 [km/h], sine wave steering (± 100 [deg], 0.25 [Hz]) on dry asphalt with the vehicle accelerating from 70 [km/h] to 120 [km/h], sine wave steering on snowy roads with acceleration from 70 [km/h] to 90 [km/h], and a step steering (100 [deg]) on snowy road at 90 [km/h]. Assessment of the algorithms was based on several statistical metrics, i.e. the RMSE, the Maximum Error (ME), the average estimation error (Mu), and the standard deviation of estimation errors σ . The results, are given in Table 11 and unequivocally demonstrate the superior performance of the proposed method. Specifically, the improvement in RMSE was significant when compared to existing methods, showing a maximum improvement of: 0.81 [deg] over the method proposed by Ghosh et al. (2018); 0.78 [deg] over the approach of You et al. (2009); 0.81 [deg] over the Deep Neural Networks (DNN) of Kim et al. (2020); 0.14 [deg] over the deep ensemble-based adaptive EKF of Kim et al. (2020); 0.06 [deg] over the

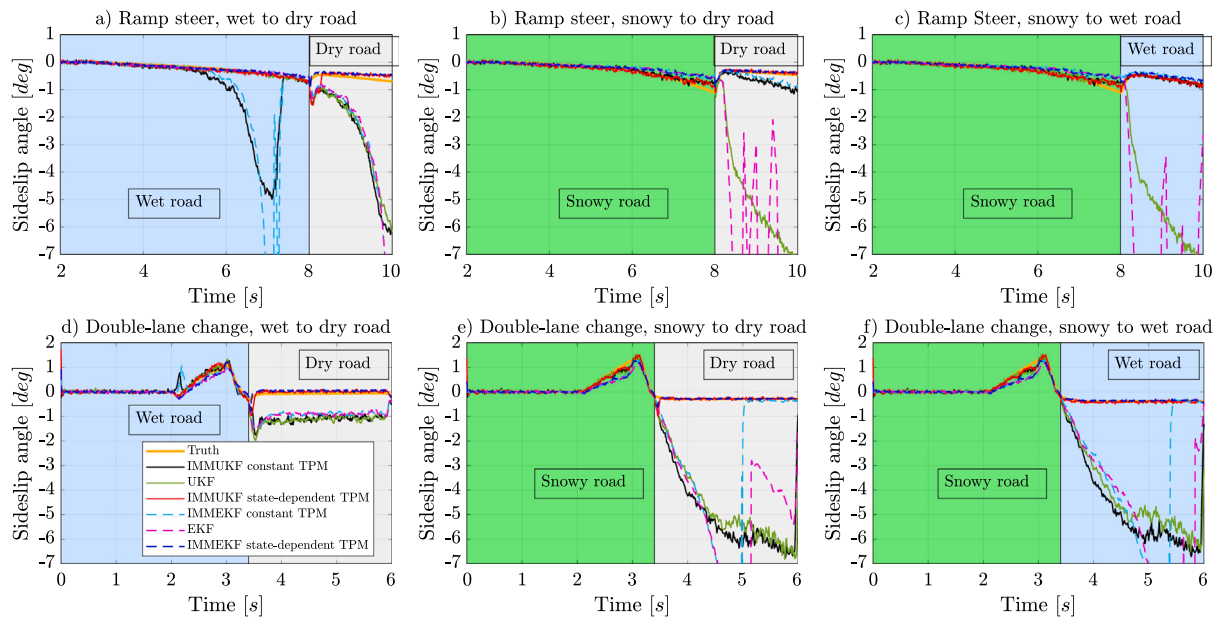


Fig. 17. Time histories of the sideslip angle estimation in a comparative analysis among an IMMUKF with constant TPM (black lines), a UKF (green lines), the proposed IMMUKF with a state-dependent TPM (red lines), an IMMEKF with constant TPM (dashed cyan lines), a EKF (dashed magenta lines), and the proposed IMMEKF with a state-dependent TPM (dashed blue lines) for: (a) ramp steer manoeuvre with a change from wet to dry in road surface; (b) ramp steer manoeuvre with a change from snowy to dry in road surface; (c) ramp steer manoeuvre with a change from snowy to wet in road surface; (d) Double-lane change with a change from wet to dry in road surface; (e) Double-lane change with a change from snowy to dry in road surface; (f) Double-lane change with a change from snowy to wet in road surface. (For interpretation of the references to colour in this figure legend, the reader is referred to the web version of this article.)

Table 10
Comparison analysis: Driving scenarios.

	Scenario	Velocity [km/h]	Time [s]
Scenario 1	Double lane change on dry asphalt road	120	10
Scenario 2	Double lane change on snowy road	120	10
Scenario 3	Sine steering (± 100 [deg], 0.25 [Hz]) on dry asphalt road	70 → 120 (+1 [m/s ²])	45
Scenario 4	Sine steering (± 100 [deg], 0.25 [Hz]) on snowy road	70 → 90 (+1 [m/s ²])	45
Scenario 5	Step steering (100 [deg]) on snowy road	90	15

deep ensemble-based adaptive UKF of Kim et al. (2020); 0.30 [deg] over the EKF; 0.26 [deg] over the UKF; 1.37 [deg] over the IMMEKF with constant TPM; and 0.72 [deg] over the IMMUKF with constant TPM. These further results solidify the standing of the IMMs with a state-dependent TPM approach, highlighting its potential as a significant advancement in vehicle dynamics and control systems. The method's ability to deliver highly accurate sideslip angle estimations across a wide spectrum of driving scenarios underscores its potential for integration into advanced vehicular safety systems, offering a substantial leap forward in ensuring vehicle stability and occupant safety under demanding driving conditions.

5.3. Results along handling tracks

The capabilities to cope with abrupt road surface condition changes are assessed and deepened by leveraging the high-fidelity co-simulation platform described in Section 4. To this aim, since the UKF-based solution has achieved better performance according to the comparative results delineated in the previous section, for the sake of brevity only the results about the estimation performance of the IMMUKF have been further investigated in the following.

The analysis focuses on two illustrative testing tracks in Figs. 18(a)–19(a), since they are typically exploited to handle vehicle test procedures. In these track scenarios, four sections are identified and highlighted with different colours to better distinguish them. Specifically, dry, damp, wet, and snowy asphalt is highlighted using black, red, blue, and green colours, respectively.

A tyre-road friction coefficient discontinuity occurs when the vehicle moves crossing from one section to another. The longitudinal and lateral driver models act directly on the throttle/brake and the steering systems in order to provide the proper command actions to drive the vehicle speed and steering wheel so as to effectively track the path. The exemplar results obtained performing a single lap of 3041 [m] are reported in Fig. 18(b) and disclose again the excellent capabilities of the proposed state-dependent IMMUKF in on-line estimating the VSA over different road surface conditions, besides striking robustness in dealing with abrupt changes of the driving environment. More specifically, the bottom of this figure depicts the probability μ_k for each of the 4 IMMUKF's modes (smoothed with moving averages), computed by the filter according to the model probability update process described in Battistini and Menegaz (2017), as a function of the state-dependent TPM. Analysing the upper and lower part of the cited figure, the transition among the mode probabilities can be easily compared with the estimation of VSA, disclosing that: in the first 40 [s] the vehicle moves on dry asphalt, and hence the mode 1 is correctly selected as the most representative; between approximately 40 and 90 [s], the road surface is damp and accordingly the mode 2 is the most reliable; from, approximately, 90 [s] to 130 [s] the wet asphalt correctly induce to consider more trustworthy the mode 3; in the last 50 [s], approximately, when at last the vehicle travels along a snowy road, the mode 4 is rightly selected. Note that, when the vehicle travels in a specific section among damp, wet, and snowy, and no steering actions occur, the proposed state-dependent IMMUKF is designed so to provide a higher reliability to the mode 1 probability, i.e. mode for dry asphalt. This justifies the increased probability of dry asphalt mode

Table 11

Comparison Analysis: results in the driving scenarios summarized in [Table 10](#). Nomenclature: RMSE - root mean square error; ME - maximum error; Mu - mean estimation error; σ - standard deviation of estimation errors. The highest performance are distinctly marked in bold.

		Scenario 1	Scenario 2	Scenario 3	Scenario 4	Scenario 5
Ghosh et al. (2018)	RMSE [deg]	0.33	0.55	0.70	0.96	0.31
	ME [deg]	3.49	1.90	3.10	4.20	4.93
	Mu [deg]	0.07	-0.05	0.12	0.21	0.09
	σ [deg]	0.33	0.55	0.69	0.93	0.30
You et al. (2009)	RMSE [deg]	0.24	0.16	0.90	0.36	0.16
	ME [deg]	0.67	0.48	1.87	0.97	0.76
	Mu [deg]	0.01	0.02	0.02	0.05	0.08
	σ [deg]	0.22	0.15	0.89	0.35	0.14
Kim et al. (2020) DNN	RMSE [deg]	0.18	0.30	0.28	0.96	0.14
	ME [deg]	1.04	0.92	1.18	3.84	1.04
	Mu [deg]	0.03	-0.04	0.02	0.09	-0.05
	σ [deg]	0.11	0.30	0.28	0.96	0.13
Kim et al. (2020) EKF + DNN	RMSE [deg]	0.11	0.09	0.26	0.18	0.09
	ME [deg]	0.29	0.20	0.48	0.36	0.21
	Mu [deg]	0.00	-0.02	0.04	0.00	-0.07
	σ [deg]	0.11	0.09	0.26	0.18	0.05
Kim et al. (2020) UKF + DNN	RMSE [deg]	0.06	0.06	0.18	0.10	0.07
	ME [deg]	0.15	0.18	0.42	0.24	0.10
	Mu [deg]	-0.01	-0.03	0.08	0.02	-0.06
	σ [deg]	0.06	0.05	0.16	0.10	0.03
EKF	RMSE [deg]	0.09	0.30	0.21	0.38	0.36
	ME [deg]	0.19	0.55	1.88	1.36	0.60
	Mu [deg]	0.04	-0.15	0.01	-0.02	-0.29
	σ [deg]	0.08	0.27	0.21	0.38	0.22
UKF	RMSE [deg]	0.16	0.28	0.26	0.35	0.32
	ME [deg]	0.33	0.54	1.78	1.30	0.52
	Mu [deg]	0.06	-0.14	0.01	-0.01	-0.26
	σ [deg]	0.15	0.25	0.26	0.35	0.19
IMMEKF constant TPM	RMSE [deg]	0.78	0.13	1.49	0.18	0.10
	ME [deg]	4.95	0.26	13.90	0.70	0.24
	Mu [deg]	0.02	-0.06	-0.10	-0.01	-0.08
	σ [deg]	0.78	0.12	1.49	0.18	0.07
IMMUKF constant TPM	RMSE [deg]	0.42	0.07	0.84	0.14	0.07
	ME [deg]	2.40	0.20	5.00	0.70	0.25
	Mu [deg]	0.06	-0.02	0.01	0.00	0.02
	σ [deg]	0.42	0.06	0.84	0.14	0.06
IMMEKF state-dependent TPM	RMSE [deg]	0.04	0.11	0.14	0.17	0.08
	ME [deg]	0.14	0.23	0.63	0.70	0.23
	Mu [deg]	-0.01	-0.05	-0.01	-0.01	-0.06
	σ [deg]	0.4	0.10	0.14	0.17	0.06
IMMUKF state-dependent TPM	RMSE [deg]	0.03	0.06	0.12	0.15	0.06
	ME [deg]	0.13	0.16	0.56	0.69	0.24
	Mu [deg]	-0.01	-0.01	0.00	0.00	0.02
	σ [deg]	0.03	0.05	0.12	0.15	0.06

from 50 [s] to 60 [s] when the road surface is in damp conditions, or, for example, around the time range between 120 [s] and 135 [s], when snowy road conditions occur. In the second handling track scenario in [Fig. 19\(a\)](#) the estimation performance exhibited by the novel state-dependent approach in both the EKF and UKF configuration are given in the presence again of four sudden changes in the asphalt conditions. The powerful estimation skills of our approach show their superiority in comparison with the other approaches already analysed, i.e. the IMM with constant TPM, in both EKF and UKF configurations, and the Kalman filter solutions (EKF and UKF), as clearly represented in [Fig. 19\(b\)](#). Note that, to improve the readability, for the IMMEKF and IMMUKF we do not provide the mode probability switching, as in the previous track scenario.

6. Conclusions

This paper has presented two novel IMM-based methods that, exploiting both the Extended and the Unscented Kalman Filter, accurately estimate the vehicle sideslip angle using available on-board sensors in different driving conditions, i.e. dry, wet, damp and snowy road asphalt, without any a priori tyre-road friction knowledge. The proposed IMM estimators are designed on the basis of a 2-DOF single-track

vehicle model with a Dugoff tyre model, suitable to obtain a simplicity in designing with a suitable accuracy in describing extreme driving manoeuvre. While the crucial point of setting the initial probabilities of the IMM's TPM is generally dealt with exploiting a priori information and/or dedicated analysis, in this paper this constrained assumption has been relaxed proposing a state-dependent TPM and a switching algorithm among models. According to this novelty, an EKF and an UKF-based IMM system have been designed, referred to as IMMEKF and IMMUKF respectively. Leveraging a high-fidelity co-simulation platform embedding the dSPACE software ASM, a Monte Carlo analysis has been carried out to compare the advantages between them, as well as with a classical IMMUKF with constant TPM, in order to evaluate the best performance and to justify the need of the state-dependent solution proposed. The comparison with respect to the constant TPM approach confirms the benefits of the proposed state-dependent TPM, since the standard deviations of estimation errors for both UKF-based and EKF-based solutions converge to lower values. More specifically, the analysis highlights that the state-dependent IMMUKF result to be the most accurate in the estimation of the yaw rate and tyres lateral force.

Finally, the effectiveness of the state-dependent IMMUKF has been tested in two handling track scenarios via the high-fidelity co-simul-

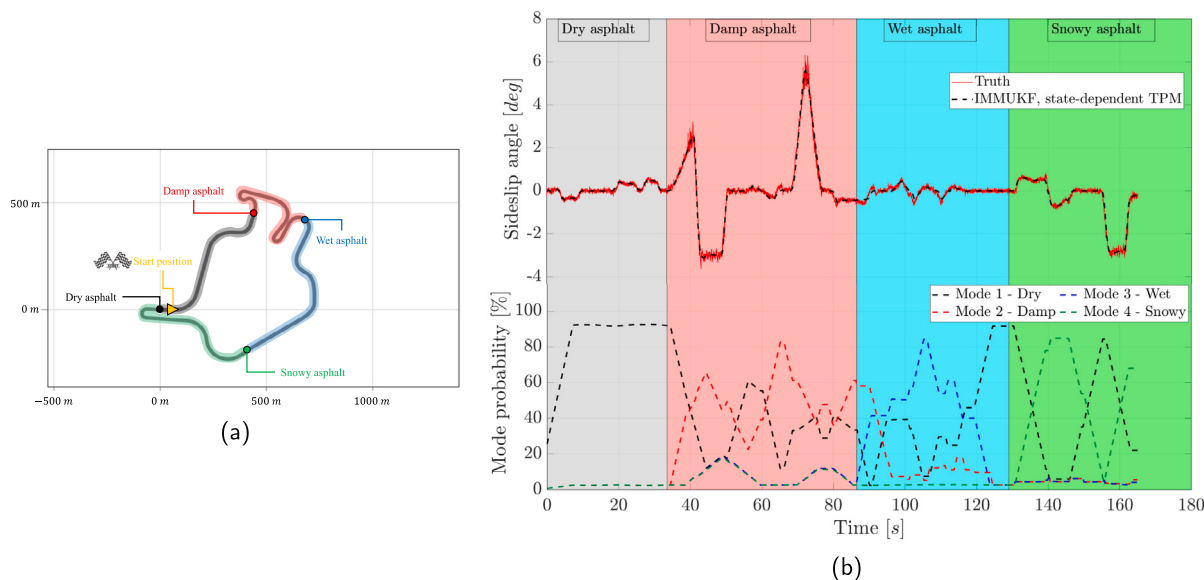


Fig. 18. (a) First Handling track; (b) time history of the vehicle sideslip angle estimation in four different road surface condition sections of the simulation scenario, i.e. black colour for the dry section, red colour for the damp section, blue colour for the wet section, and green colour for the snowy section. (For interpretation of the references to colour in this figure legend, the reader is referred to the web version of this article.)

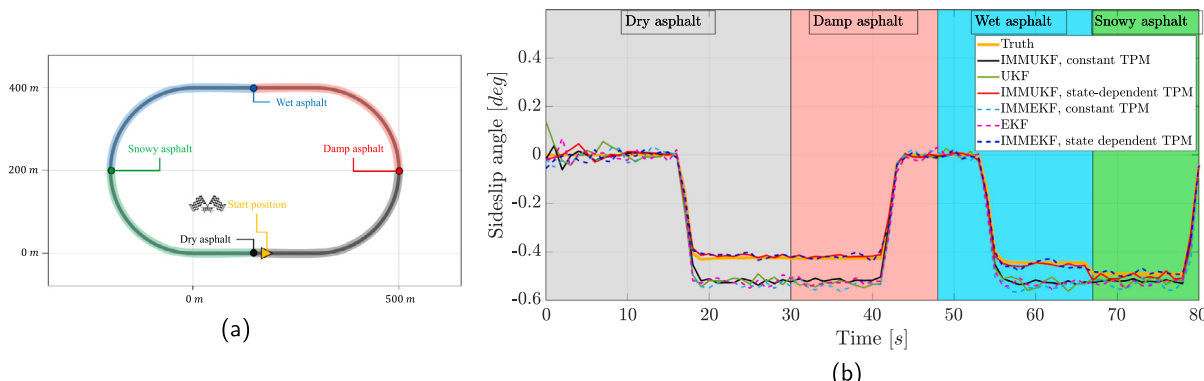


Fig. 19. (a) Second Handling track; (b) time history of the vehicle sideslip angle estimation in four different road surface condition sections of the simulation scenario, i.e. black colour for the dry section, red colour for the damp section, blue colour for the wet section, and green colour for the snowy section. (For interpretation of the references to colour in this figure legend, the reader is referred to the web version of this article.)

ation platform, disclosing the VSA estimation accuracy in a real driving environment, dealing with abruptly changes of road surface conditions. Future works include the effectiveness of the proposed approach in real-world experiments.

CRediT authorship contribution statement

Francesco Tufano: Writing – review & editing, Writing – original draft, Validation, Software, Methodology, Investigation, Formal analysis, Conceptualization. **Dario Giuseppe Lui:** Writing – review & editing, Writing – original draft, Validation, Software, Methodology, Investigation, Formal analysis, Conceptualization. **Simone Battistini:** Writing – review & editing, Writing – original draft, Validation, Software, Methodology, Investigation, Formal analysis, Conceptualization. **Renato Brancati:** Writing – review & editing, Writing – original draft, Validation, Software, Methodology, Investigation, Formal analysis, Conceptualization. **Basilio Lenzo:** Writing – review & editing, Writing – original draft, Validation, Software, Methodology, Investigation, Formal analysis, Conceptualization. **Stefania Santini:** Writing – review & editing, Writing – original draft, Validation, Software, Methodology, Investigation, Formal analysis, Conceptualization.

Declaration of competing interest

The authors declare that they have no known competing financial interests or personal relationships that could have appeared to influence the work reported in this paper.

Acknowledgements

This research was partially funded by the COP Research and Innovation 2014–2020 - Axis I - Investment in Human Capital - Action I.1 Innovative Industrial Doctorates, project “XIL Simulations: Methodologies for Check and Validation of Systems for Autonomous Driving” (CUP: E65F19001220007). The project was executed in collaboration with Stellantis N.V.

References

- Battistini, S., Brancati, R., Lui, D. G., & Tufano, F. (2022). Enhancing ADS and ADAS under critical road conditions through vehicle sideslip angle estimation via unscented Kalman filter-based interacting multiple model approach. In *The international conference of iFToMM ITALY* (pp. 450–460). Springer.
- Battistini, S., & Menegaz, H. M. (2017). Interacting multiple model unscented filter for tracking a ballistic missile during its boost phase. In *2017 IEEE aerospace conference* (pp. 1–8). IEEE.

- Blom, H. A. P. (1984). An efficient filter for abruptly changing systems. In *The 23rd IEEE conference on decision and control* (pp. 656–658). IEEE.
- Bonfitto, A., Feraco, S., Tonoli, A., & Amati, N. (2020). Combined regression and classification artificial neural networks for sideslip angle estimation and road condition identification. *Vehicle System Dynamics*, 58(11), 1766–1787.
- Brancati, R., & Tufano, F. (2022). Indirect estimation of tire pressure on several road pavements via interacting multiple model approach. *Machines*, 10(12), 1221.
- Caiazzo, B., Lui, D. G., Petrillo, A., & Santini, S. (2021). Distributed double-layer control for coordination of multiplatoons approaching road restriction in the presence of IoT communication delays. *IEEE Internet of Things Journal*, 9(6), 4090–4109.
- Candeli, A., De Tommasi, G., Lui, D. G., Mele, A., Santini, S., & Tartaglione, G. (2022). A deep deterministic policy gradient learning approach to missile autopilot design. *IEEE Access*, 10, 19685–19696.
- Chindamo, D., Lenzo, B., & Gadola, M. (2018). On the vehicle sideslip angle estimation: a literature review of methods, models, and innovations. *Applied Sciences*, 8(3), 355.
- Chowdhri, N., Ferranti, L., Iribarren, F. S., & Shyrokau, B. (2021). Integrated nonlinear model predictive control for automated driving. *Control Engineering Practice*, 106, Article 104654.
- Coppola, A., Lui, D. G., Petrillo, A., & Santini, S. (2021). Distributed fixed-time leader-tracking control for heterogeneous uncertain autonomous connected vehicles platoons. In *2021 29th mediterranean conference on control and automation* (pp. 554–559). IEEE.
- Coppola, A., Lui, D. G., Petrillo, A., & Santini, S. (2022). Eco-driving control architecture for platoons of uncertain heterogeneous nonlinear connected autonomous electric vehicles. *IEEE Transactions on Intelligent Transportation Systems*.
- de Nola, F., Giardiello, G., Gimelli, A., Molteni, A., Muccillo, M., & Picariello, R. (2017). *A model-based computer aided calibration methodology enhancing accuracy, time and experimental effort savings through regression techniques and neural networks*. SAE Technical Paper.
- Demerly, J. D., & Youcef-Toumi, K. (2000). *Non-linear analysis of vehicle dynamics (NAVDyn): A reduced order model for vehicle handling analysis*: Technical report, SAE Technical Paper.
- Di Biase, F., Lenzo, B., & Timpone, F. (2020). Vehicle sideslip angle estimation for a heavy-duty vehicle via extended Kalman filter using a rational tyre model. *IEEE Access*, 8, 142120–142130.
- Di Vaio, M., Falcone, P., Hult, R., Petrillo, A., Salvi, A., & Santini, S. (2019). Design and experimental validation of a distributed interaction protocol for connected autonomous vehicles at a road intersection. *IEEE Transactions on Vehicular Technology*, 68(10), 9451–9465.
- Doumiati, M., Victorino, A. C., Charara, A., & Lechner, D. (2010). Onboard real-time estimation of vehicle lateral tire-road forces and sideslip angle. *IEEE/ASME Transactions on Mechatronics*, 16(4), 601–614.
- Dugoff, H., Fancher, P. S., & Segel, L. (1970). An analysis of tire traction properties and their influence on vehicle dynamic performance. *SAE Transactions*, 1219–1243.
- Fiengo, G., Lui, D. G., Petrillo, A., Santini, S., & Tufo, M. (2019). Distributed robust PID control for leader tracking in uncertain connected ground vehicles with V2V communication delay. *IEEE/ASME Transactions on Mechatronics*, 24(3), 1153–1165.
- Garcia, R., Pardal, P., Kuga, H., & Zanardi, M. (2019). Nonlinear filtering for sequential spacecraft attitude estimation with real data: Cubature Kalman filter, unscented Kalman filter and extended Kalman filter. *Advances in Space Research*, 63(2), 1038–1050.
- Ghosh, J., Tonoli, A., & Amati, N. (2018). *A deep learning based virtual sensor for vehicle sideslip angle estimation: experimental results*: Technical report, SAE Technical Paper.
- Guiggiani, M. (2014). *The science of vehicle dynamics* (p. 15). Pisa, Italy: Springer Netherlands.
- Guo, Z., Dong, C., Cai, Y., & Yu, Z. (2015). Time-varying transition probability based IMM-SRCKF algorithm for maneuvering target tracking. *Systems Engineering and Electronics*, 37(1), 24–30.
- Jasiński, M. (2019). A generic validation scheme for real-time capable automotive radar sensor models integrated into an autonomous driving simulator. In *2019 24th international conference on methods and models in automation and robotics* (pp. 612–617). IEEE.
- Jin, X., & Yin, G. (2015). Estimation of lateral tire-road forces and sideslip angle for electric vehicles using interacting multiple model filter approach. *Journal of the Franklin Institute*, 352(2), 686–707.
- Jing, C., Shu, H., Shu, R., & Song, Y. (2022). Integrated control of electric vehicles based on active front steering and model predictive control. *Control Engineering Practice*, 121, Article 105066.
- Joa, E., Yi, K., & Hyun, Y. (2019). Estimation of the tire slip angle under various road conditions without tire-road information for vehicle stability control. *Control Engineering Practice*, 86, 129–143.
- Joubert, N., Reid, T. G., & Noble, F. (2020). Developments in modern GNSS and its impact on autonomous vehicle architectures. In *2020 IEEE intelligent vehicles symposium* (pp. 2029–2036). IEEE.
- Kiencke, U., & Nielsen, L. (2005). *Automotive control systems: For engine, driveline, and vehicle*. Springer.
- Kim, D., Min, K., Kim, H., & Huh, K. (2020). Vehicle sideslip angle estimation using deep ensemble-based adaptive Kalman filter. *Mechanical Systems and Signal Processing*, 144, Article 106862.
- Lee, I. H., & Park, C. G. (2022). A two-stage transition correction function for adaptive Markov matrix in IMM algorithm. In *2022 25th international conference on information fusion* (pp. 1–8). IEEE.
- Li, J., & Zhang, J. (2016). Vehicle sideslip angle estimation based on hybrid Kalman filter. *Mathematical Problems in Engineering*, 2016.
- Liao, Y.-W., & Borrelli, F. (2019). An adaptive approach to real-time estimation of vehicle sideslip, road bank angles, and sensor bias. *IEEE Transactions on Vehicular Technology*, 68(8), 7443–7454.
- MacAdam, C. C. (1981). Application of an optimal preview control for simulation of closed-loop automobile driving. *IEEE Transactions on Systems, Man, and Cybernetics*, 11(6), 393–399.
- Madhusudhanan, A. K., Corno, M., & Holweg, E. (2016). Vehicle sideslip estimator using load sensing bearings. *Control Engineering Practice*, 54, 46–57.
- Menegaz, H. M., & Battistini, S. (2018). Switching multiple model filter for boost-phase missile tracking. *IEEE Transactions on Aerospace and Electronic Systems*, 54(5), 2547–2553.
- Menegaz, H. M., Ishihara, J. Y., Borges, G. A., & Vargas, A. N. (2015). A systematization of the unscented Kalman filter theory. *IEEE Transactions on Automatic Control*, 60(10), 2583–2598.
- Musa, A., Pipicelli, M., Spano, M., Tufano, F., De Nola, F., Di Blasio, G., et al. (2021). A review of model predictive controls applied to advanced driver-assistance systems. *Energies*, 14(23), 7974.
- Pacejka, H. (2005). *Tire and vehicle dynamics*. Elsevier.
- Panáček, V., Semela, M., Adamec, V., & Schüllerová, B. (2016). Impact of usable coefficient of adhesion between tyre and road surface by modern vehicle on its dynamics while driving and braking in the curve. *Transport*, 31, 142–146.
- Park, G. (2022). Vehicle sideslip angle estimation based on interacting multiple model Kalman filter using low-cost sensor fusion. *IEEE Transactions on Vehicular Technology*.
- Petrillo, A., Prati, M. V., Santini, S., & Tufano, F. (2023). Improving the NOx reduction performance of an euro VI d SCR system in real-world condition via nonlinear model predictive control. *International Journal of Engine Research*, 24(3), 823–842.
- Ping, X., Cheng, S., Yue, W., Du, Y., Wang, X., & Li, L. (2020). Adaptive estimations of tyre-road friction coefficient and body's sideslip angle based on strong tracking and interactive multiple model theories. *Proceedings of the Institution of Mechanical Engineers, Part D (Journal of Automobile Engineering)*, 234(14), 3224–3238.
- Ray, L. R. (1997). Nonlinear tire force estimation and road friction identification: Simulation and experiments. *Automatica*, 33(10), 1819–1833.
- Russo, M., Russo, R., & Volpe, A. (2000). Car parameters identification by handling manoeuvres. *Vehicle System Dynamics*, 34(6), 423–436.
- Selmanaj, D., Corno, M., Panzani, G., & Savaresi, S. M. (2017). Vehicle sideslip estimation: A kinematic based approach. *Control Engineering Practice*, 67, 1–12.
- Strano, S., & Terzo, M. (2018). Constrained nonlinear filter for vehicle sideslip angle estimation with no a priori knowledge of tyre characteristics. *Control Engineering Practice*, 71, 10–17.
- Tsunashima, H., Murakami, M., & Miyata, J. (2006). Vehicle and road state estimation using interacting multiple model approach. *Vehicle System Dynamics*, 44(sup1), 750–758.
- Villano, E., Lenzo, B., & Sakhnevych, A. (2021). Cross-combined UKF for vehicle sideslip angle estimation with a modified dugoff tire model: design and experimental results. *Mecanica*, 56(11), 2653–2668.
- Xia, X., Hang, P., Xu, N., Huang, Y., Xiong, L., & Yu, Z. (2021). Advancing estimation accuracy of sideslip angle by fusing vehicle kinematics and dynamics information with fuzzy logic. *IEEE Transactions on Vehicular Technology*, 70(7), 6577–6590.
- Xie, G., Sun, L., Wen, T., Hei, X., & Qian, F. (2019). Adaptive transition probability matrix-based parallel IMM algorithm. *IEEE Transactions on Systems, Man, and Cybernetics: Systems*, 51(5), 2980–2989.
- Xu, Y., Zhang, W., Tang, W., Liu, C., Yang, R., He, L., et al. (2022). Estimation of vehicle state based on IMM-AUKF. *Symmetry*, 14(2), 222.
- Yoon, J.-H., & Peng, H. (2013). Robust vehicle sideslip angle estimation through a disturbance rejection filter that integrates a magnetometer with GPS. *IEEE Transactions on Intelligent Transportation Systems*, 15(1), 191–204.
- You, S.-H., Hahn, J.-O., & Lee, H. (2009). New adaptive approaches to real-time estimation of vehicle sideslip angle. *Control Engineering Practice*, 17(12), 1367–1379.
- Zal, P. (2023). Automobile catalog. https://www.automobile-catalog.com/car/2018/2629355/alfa Romeo_stelvio_quadrifoglio_automatic.html. (Accessed: 06 November 2023).